

A Robotic System for Photopatterning of Freeform Surfaces

by

Adam G. Stevens

B.S.E., Mechanical Engineering
University of Michigan, 2013

Submitted to the Department of Mechanical Engineering
in Partial Fulfillment of the Requirements for the Degree of

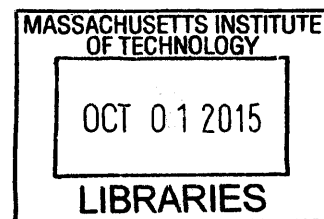
MASTER OF SCIENCE IN MECHANICAL ENGINEERING

at the

MASSACHUSETTS INSTITUTE OF TECHNOLOGY

September 2015

ARCHIVES



Copyright 2015 Massachusetts Institute of Technology. All rights reserved.



Signature redacted

Signature of Author: _____

Department of Mechanical Engineering
August 21, 2015



Signature redacted

Certified by: _____


A. John Hart
Associate Professor of Mechanical Engineering
Thesis Supervisor


Signature redacted

Accepted by: _____


David E. Hardt
Chairman, Committee on Graduate Students

intentionally blank

A Robotic System for Photopatterning of Freeform Surfaces

by

Adam G. Stevens

Submitted to the Department of Mechanical Engineering
on August 21, 2015 in Partial Fulfillment of the
Requirements for the Degree of Master of Science in
Mechanical Engineering

ABSTRACT

Additive manufacturing by photopolymerization (e.g., stereolithography) is attractive due to its high resolution and its compatibility with soft and hard polymers, composites, and biomaterials. While traditional stereolithography machines are designed to build on planar substrates, patterning of non-planar surfaces would enable integration of new functionality onto existing objects for applications such as structurally integrated sensors, conformal electronics, and customized medical implants. This thesis presents the design, construction, and initial performance evaluation of a robotic system capable of maskless photopatterning on objects having complex curvature and dimensions ranging from centimeters to meters.

The system incorporates a six-axis serial robot arm, a high-precision rotary stage, a custom-built DLP-based end effector, and custom software that coordinates and controls the system. The workpiece is patterned by first digitally triangulating the surface with a 3D scanner and associating the location of each triangle in the digital space with the corresponding location on the workpiece surface in real space. Subsequently, the area enclosed by each triangle is associated with a user-specified texture photomask. The large-area photopattern is then fabricated by sequentially exposing each individual textured triangle in the photomask as the robot steps to each corresponding location on the workpiece surface, which is coated with a photocurable polymer.

By measuring patterning results on a test object, the system was determined to have a positioning accuracy over a subsection of the working volume of $330\mu\text{m}$ and a repeatability of $20\mu\text{m}$ was measured by a motion test. The system positioning accuracy is limited by performance of the actuators and the kinematics of the manipulator. System patterning rate is limited by the power output of the light source. The system's performance is demonstrated by patterning a 21cm diameter sphere with a map of the Earth and performing a preliminary test on the patellar surface of an anatomical femur model. Future work will focus on improving the system accuracy by mapping the workspace using a coordinate measuring machine and increasing throughput by a combination of increased optical power and more efficient use of the projection field of view. The system will also be investigated as an enabling technology for deterministically patterning cartilage cells onto joint surfaces or three-dimensional anatomical models.

Thesis Supervisor: A. John Hart

Title: Associate Professor of Mechanical Engineering

intentionally blank

Acknowledgements

I would like to thank Professor A. John Hart and Dr. Ryan Oliver for their insight and guidance during my studies and while writing this thesis.

This project began as my senior design project at the University of Michigan in the fall of 2012.

I would like to acknowledge the contributions to this project of:

Professor Jyoti Mazumder, our faculty advisor;

Professor A. John Hart, our faculty sponsor;

my teammates Chad Archer, Casey Boyle, and Jenna Garber;

and our advisors Drs. Ryan Oliver and Erik Polsen.

In graduate school I had the pleasure of working with undergraduates Jieyuan Wu and Lillian Chin, both of whom contributed to the software and hardware development.

intentionally blank

Contents

Chapter 1: Introduction and Background	9
Chapter 2: Robotic Manipulator Designs and Their Uses in Additive Manufacturing	15
ROBOTICS OVERVIEW	15
OPPORTUNITIES FOR ROBOTICS IN ADDITIVE MANUFACTURING	22
CONCLUSIONS.....	26
Chapter 3: Design and Operation of a Robotic System for Photopatterning of Freeform Surfaces	29
SYSTEM DESIGN OVERVIEW	29
SYSTEM DETAILS	33
SYSTEM CALIBRATION.....	50
CONCLUSIONS.....	54
Chapter 4: System Characterization and Demonstration	57
MEASUREMENT OF PROJECTION LITHOGRAPHY RESOLUTION.....	57
MEASUREMENT OF THE ACCURACY AND REPEATABILITY OF THE MOTION SYSTEM..	61
LARGE-SCALE PATTERNING OF A CONSTANT CURVATURE SURFACE.....	64
PATTERNING ON SURFACES OF COMPLEX CURVATURE.....	66
Chapter 5: Conclusions and Future Work	75
Bibliography	79

intentionally blank

Chapter 1: Introduction and Background

Additive manufacturing has gained traction as a viable technique for manufacturing rapid prototypes and parts that cannot be fabricated by traditional manufacturing. The key principle of additive manufacturing is the concept of building objects layer-by-layer from 3D model data.¹ One of the first examples of additive manufacturing was proposed by Kodama,² who used layer-by-layer curing of a photopolymer to generate simple three-dimensional polymer parts. Shortly thereafter a similar method, termed stereolithography, was patented by Hull³ in the United States. However, to date most techniques, such as fused material deposition (FDM), only enable fabrication of single material polymer parts with weak bonds and functionality.^{1,4}

Relatively little work has been done to use additive manufacturing to integrate new functionality onto existing objects.⁵ This thesis describes an advanced manufacturing method for applying 2D patterns directly onto solid freeform surfaces via maskless photopatterning.

Current photopatterning methods fall into several categories, including mask, direct-write, and transfer printing. Mask-based methods include contact mask⁶⁻⁸ and projection lithography whereby a patterned mask is used to selectively expose and transfer the pattern into a photoactive polymer.⁹⁻¹¹ Direct-write lithography involves rastering a photosensitive polymer with a radiation beam, often in the form of electron-beams,^{12,13} ion beams,^{14,15} or lasers.^{16,17} Finally, transfer methods such as soft lithography usually involve an elastomeric stamp such as PDMS¹⁸ to transfer micro- to nano-scale features onto planar substrates.^{18,19} The maturity of the above planar photolithography processes has enabled the miniaturization of semiconductor electronics, digital micromirror devices, and engineered surfaces such as directed cell growth and superhydrophobicity (Figure 1).

The abovementioned techniques are generally constrained to planar substrates, however some of the techniques have been extended onto surfaces of simple curvature. Soft lithography has been used to fabricate patterns and functional electronics on curved substrates.^{20,21} Another approach is to fabricate planar stretchable and flexible electronics on PDMS that are later transferred and conformally applied to a three-dimensional target object; for example this has been demonstrated for a glove-like pericardium for in-situ use during surgery.²² Also, contact mask-based lithography has been performed on simple curved surfaces using conformal CVD resist with a flexible mask.²³ Finally, direct-write lithography has recently been applied to 3D surface patterning applications using rastered laser beams to pattern conductive traces onto freeform objects for use in compact electronic devices.²⁴⁻²⁶ Figure 2 details some of the above demonstrations.

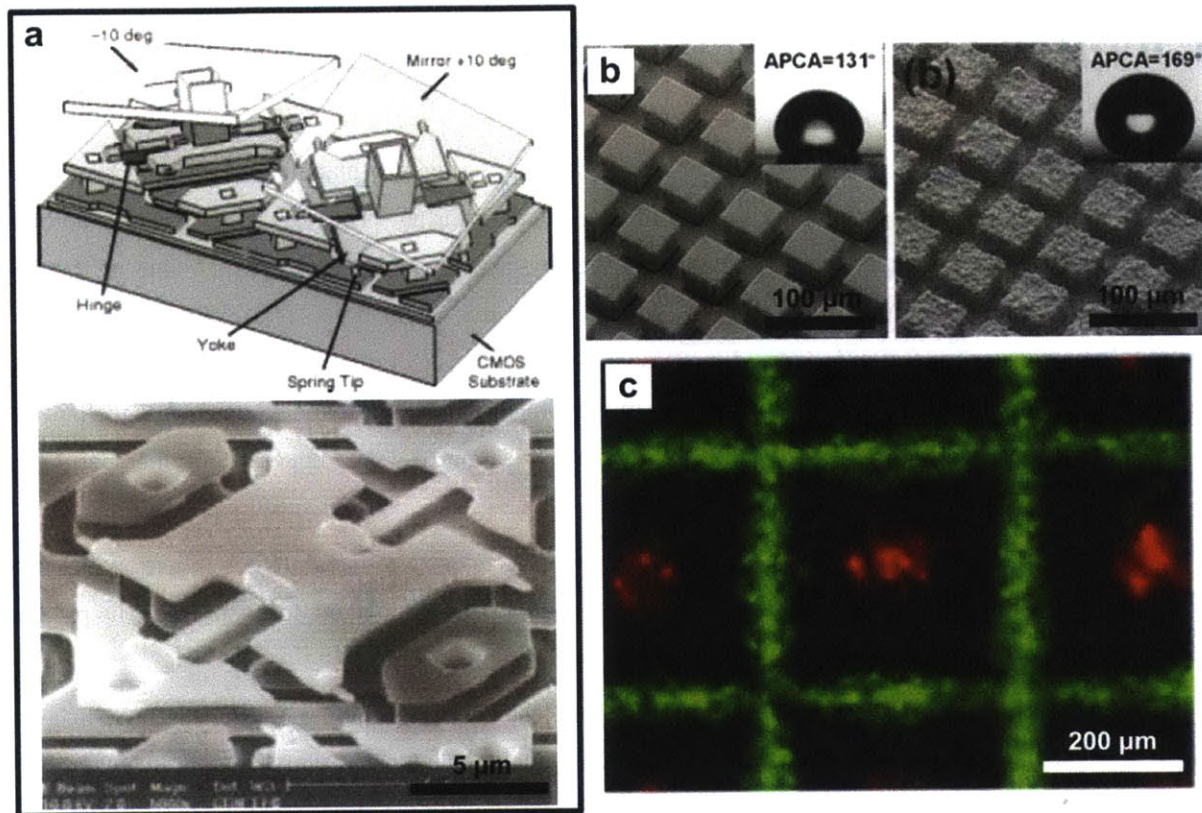


Figure 1: Applications of planar lithographic processes: a) Texas Instruments Digital Light Processing (DLP) optoelectromechanical system;²⁷ b) Wettability control via surface microstructures;²⁸ c) Templated, compartmentalized cell growth via soft lithography.²⁹

This thesis presents a robotic system capable of patterning freeform curved objects at multiple scales over large areas via robotics-enhanced direct write additive manufacturing. I discuss the design details necessary to combine robotics and photopatterning with the aim to overcome limitations in patternable geometry by using a seven-axis robotic lithography system to extend the microlithography work envelope into three spatial dimensions.

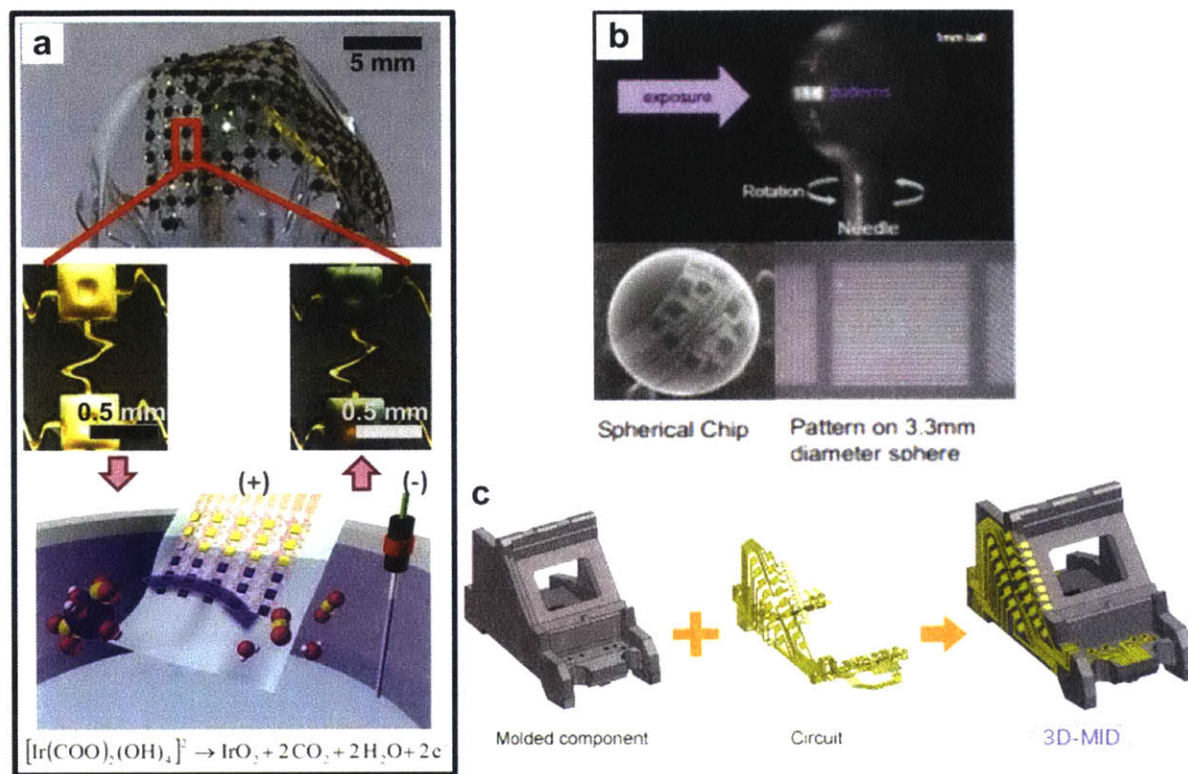


Figure 2: Applications of patterning processes to three-dimensional objects: a) Compliant pH-sensing heart sheath for use during surgery; b) Aiscent Technology's direct-write laser lithography system for creating spherical integrated circuits; c) Patterning of conductive traces directly on molded polymer parts via the 3D-MID (Mold Interconnect Device) process.

The remainder of this thesis is organized as follows:

- **Chapter 2:** The groundwork for understanding the benefits and limitations of robotics in additive manufacturing is laid by examining the capabilities of existing robotic motion systems.
- **Chapter 3:** The design of a robotic system for photopatterning freeform surfaces is presented. Mechanical and optical design is detailed, followed by a verification of the limits of the robotic system as described in Chapter 2. The control software is reviewed in detail along with a step-by-step discussion of the system operation procedure.
- **Chapter 4:** As an example application of three dimensional patterning, a sphere is patterned with a map of the Earth. Patterning on surfaces of both positive and negative curvature is also discussed.

- **Chapter 5:** The work is concluded and future improvements are discussed, including improvements in positioning accuracy, throughput, and design of a new end effector for depositing three-dimensional graded structures on freeform substrates.

intentionally blank

intentionally blank

Chapter 2: Robotic Manipulator Designs and Their Uses in Additive Manufacturing

This chapter discusses the use of motion systems in additive manufacturing, starting with a brief overview of common machine elements followed by a description of different robot categories and applications. Technical capabilities are compared for different systems, showing the tradeoffs between performance metrics such as speed and repeatability. The chapter closes with a discussion of robotic applications at the forefront of additive manufacturing.

ROBOTICS OVERVIEW

This thesis defines a robot as any automated motion system that is capable of motion in two or more spatial dimensions. Using this definition, robots find applications in a variety of industrial and commercial processes, including multi-degree-of-freedom computer numeric controlled (CNC) milling machines,³⁰ assembly lines,³¹ material handling,³² domestic chores,³³ and healthcare.³⁴ This subsection provides an overview of existing commercially available robotics technologies.

One of the primary limitations in applying commercial robotics to additive manufacturing is system accuracy. Repeatability is of primary importance for conventional manufacturing techniques involving predefined work routines repeated every manufacturing cycle. In contrast, additive manufacturing requires that accuracy and repeatability be maintained throughout the work envelope of the robot since toolpaths are generated offline from digital model information. As a result, additive manufacturing cannot rely solely on high system repeatability since each motion path is only performed once for each part.³⁵ In general, motion system accuracy is much lower than repeatability unless complicated calibration procedures are performed, but calibration procedures are not standardized, so the operator has to invest significant time and money in the process.

Most robotic systems involve series-mounted actuators, which can be modeled using matrices to determine robot pose as a function of joint angles. There are several popular approaches involving constructs known as homogeneous transform matrices (HTMs).^{36,37} In the HTM method, a given pose is described by a product of successive matrices describing the orientation of the i^{th} link relative to the $(i-1)^{\text{th}}$ link. **Eq. 1** shows a typical H matrix describing a rotation and translation, composed of submatrices $R_{i3 \times 3}$, a rotation matrix; $P_{i3 \times 1}$, a translation vector; $0_{i1 \times 3}$, a row vector of zeros; and the scalar 1. **Eq. 2** shows how the pose is calculated for a robot described by n homogeneous transform matrices.

$$H_i^{i-1} = \begin{bmatrix} R_{i3x3} & P_{i3x1} \\ 0_{i1x3} & 1 \end{bmatrix} \quad \text{Eq. 1}$$

$$T = \prod_1^n H_i^{i-1} \quad \text{Eq. 2}$$

By tabulating the relative position and orientation of each joint in a robot, the HTM matrices can be used to investigate the sensitivity of a robot design to manufacturing and compliance errors. In turn, this enables controlling the most sensitive elements in the assembly in order to increase system performance.

Basic Machine Elements

Basic motion elements for robotics include rotary and linear actuators (which generate motion) and transmissions (which transmit or convert motion). Rotary actuators and transmissions come in a variety of forms, common ones include geared rotary stages,³⁸ direct drive motors,³⁹ and piezoelectric rotary stages (which use one or more piezo elements in an inch-worm fashion to turn a stage).⁴⁰⁻⁴² Linear actuators include lead screws,⁴³ ball screws,⁴⁴ piezoelectrics,⁴⁵ rack-and-pinion assemblies,⁴⁶ and linear motors.⁴⁷ See Figure 3a for select examples. Fundamentally, precision of the above actuators is a function of manufacturing tolerances and design. Given the repeatability is suitable for the application, accuracy can then be achieved by calibrating the actuator against known metrics.⁴⁸

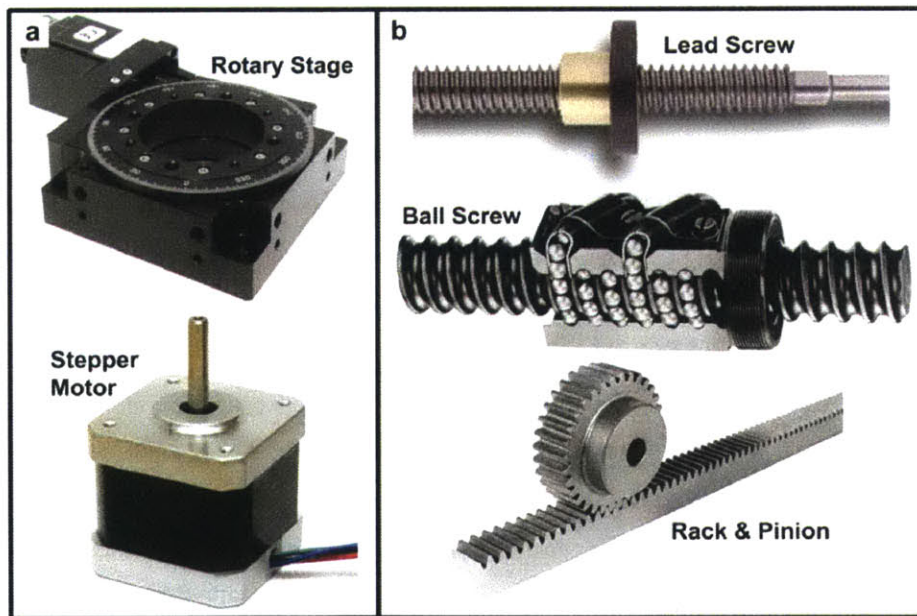


Figure 3: Mechanical elements used to form automated systems: a) A selection of rotary actuators, here a geared rotary stage⁴⁹ and stepper motor;⁵⁰ and b) Actuators that convert rotation to translation.⁵¹⁻⁵³

A diverse variety of motion elements can be combined with sensors and controllers to yield robotic systems. Some of the most common configurations are detailed below and in Figure 4, according to category.

Cartesian Gantry

Gantry systems were invented over one hundred years ago⁵⁴ with specific designs having advanced to the point of nanometer-level accuracy.⁵⁵ Gantry systems typically consist of two to three linear motion systems mounted mutually orthogonal and in series to one another. This configuration allows for straightforward programming of the robot motion, as motion in the X, Y, and Z directions is intuitively associated with a specific robot axis.

Articulated Arms

Commonly seen in manufacturing environments, articulated arms usually consist of four to six rotary joints combined in series. Six-axis articulated arms and four-axis SCARA (*Selective Compliance Articulated Robot Arm*) robots are the most common type (Figure 4). Programming is less straightforward, as the correspondence between joint actuation and direction of travel isn't direct, requiring a technique known as inverse kinematics, where a mathematical description of the robot joints is used to determine the joint angles required to reach a given position.⁵⁶ Most systems come with a user-friendly software package, allowing the user to specify translations in world coordinates without knowledge of the inverse kinematics required.

Parallel Actuators

Parallel actuator systems are frequently used in pick-and-place operations, such as populating printed circuit boards with integrated circuit devices. The parallel four-bar linkage configuration enables high speed and precision at the expense of payload capacity. Delta robots are one variant (Figure 4b) commonly seen in the food packaging industry due to the fast cycle times. Alternatively, the Stewart platform (Figure 4b) uses linear actuators rather than linkages, with piezo-based models trading speed for accuracy--several models are capable of nanometer-level performance.⁵⁷

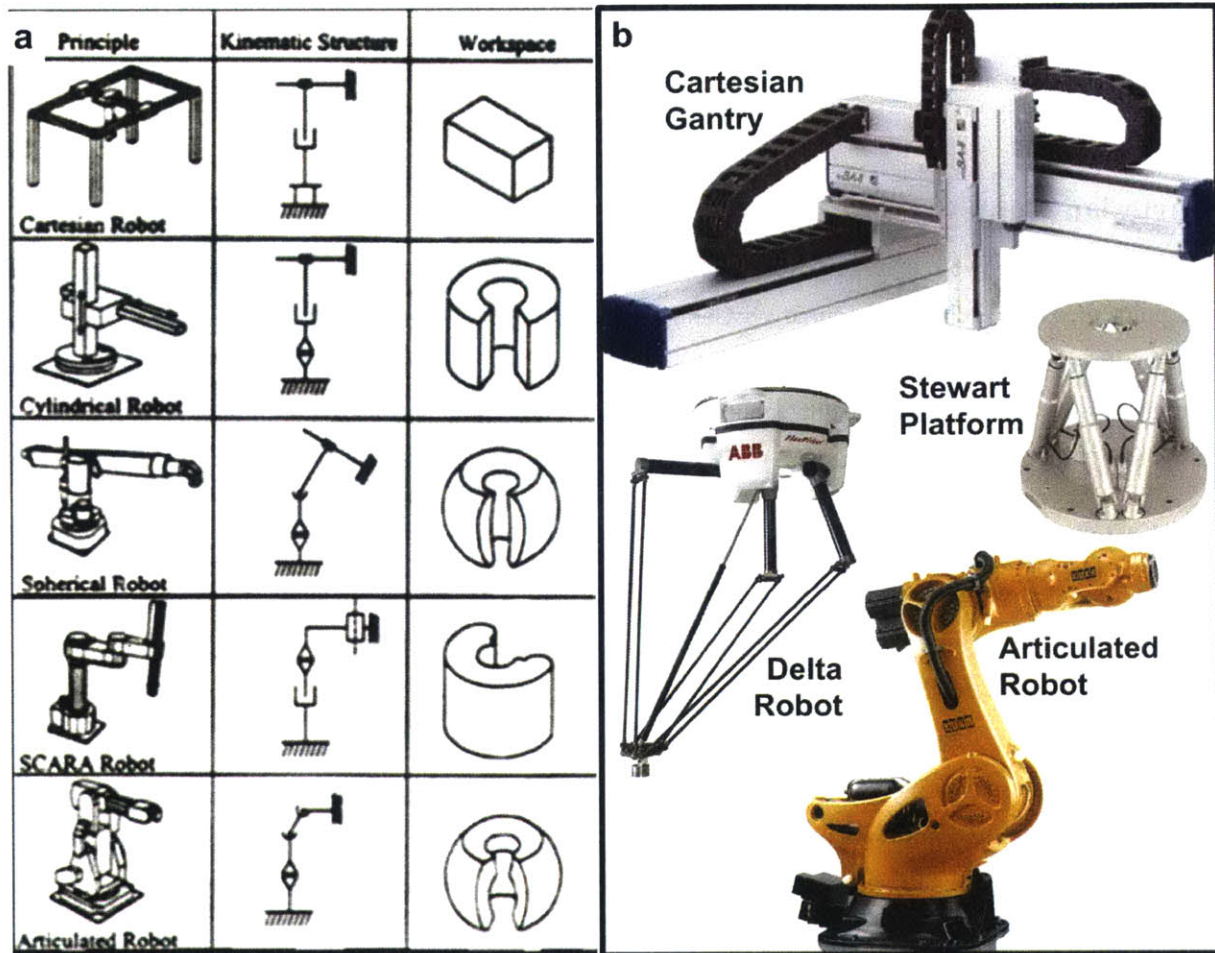


Figure 4: There are a variety of robot categories, each with different layouts and working volumes: a) A table of categories showing the general appearance, joint configuration, and workspace of each category;⁵⁸ b) Examples of modern robots in select categories.⁵⁹⁻⁶²

Performance

Performance metrics include load capacity, repeatability, work envelope or reach, and speed. Figure 5 and Figure 6 compare robot load capacity and reach to repeatability. Note that robots of a similar configuration oftentimes have similar performance. Figure 7 shows an approximate comparison between robot speed and repeatability, grouped by category. Quantitatively determining robot speed is a difficult task, because no widely-used standards exist and for a given robot the maximum speed can vary throughout the working volume as joint configurations change. All graphs are indicative of the capabilities for commercially available systems, not the maximum performance.

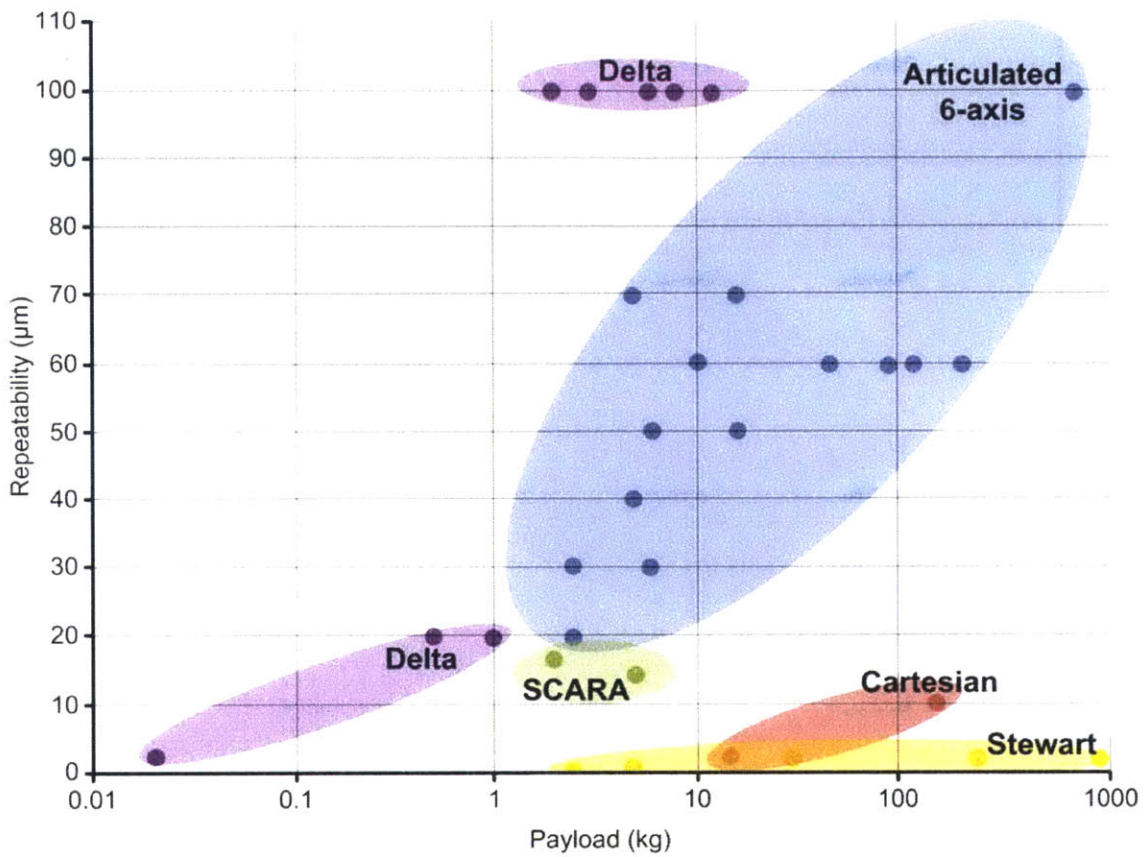


Figure 5: Given a robot configuration type, robot repeatability is largely independent of payload, with the exception of articulated robots that include cantilevered joints in the kinematic chain. These show increasing repeatability with increasing load capacity.^{63-74,75-83,52-55,88-95}

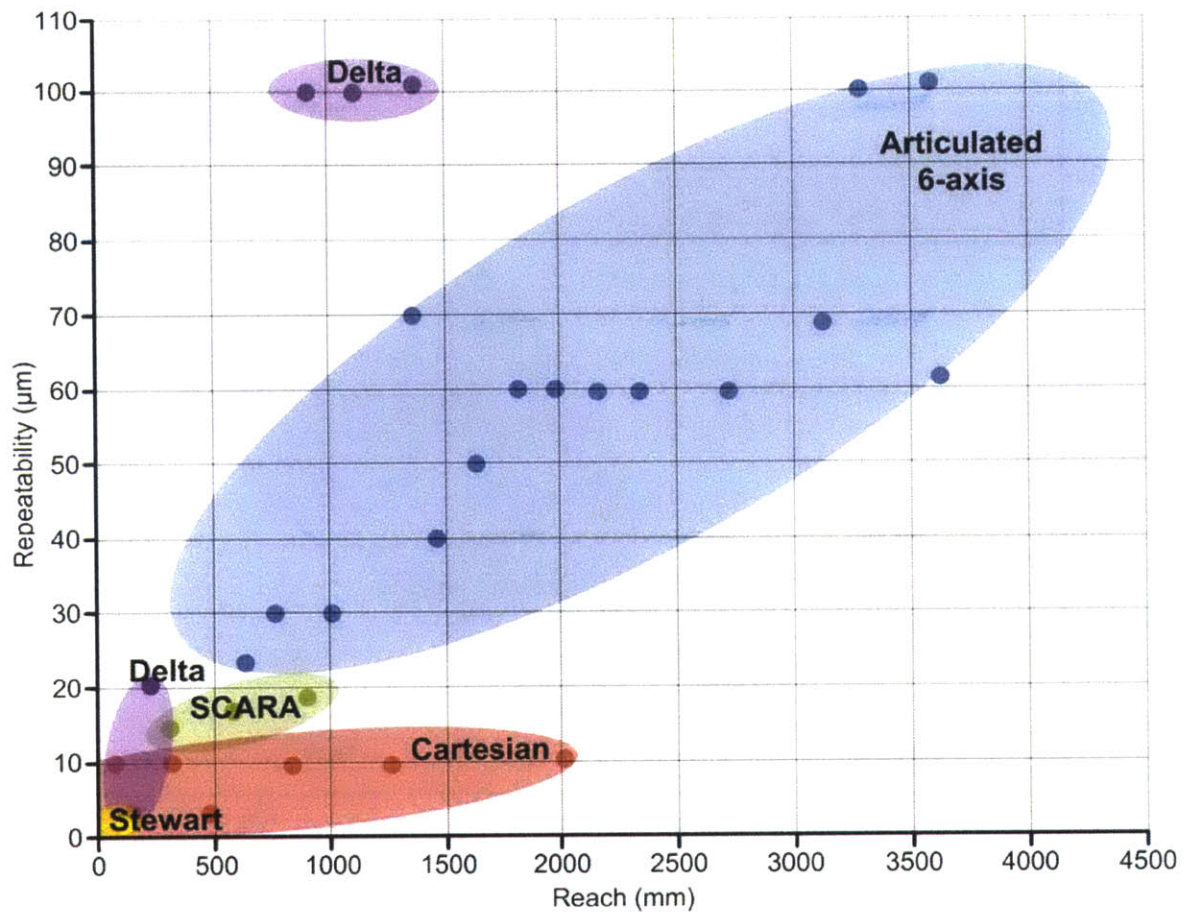


Figure 6: Comparison of commercially available robots in different categories shows the general correlation between increasing reach and increasing maximum repeatability.^{31-52,52-55,88-95}

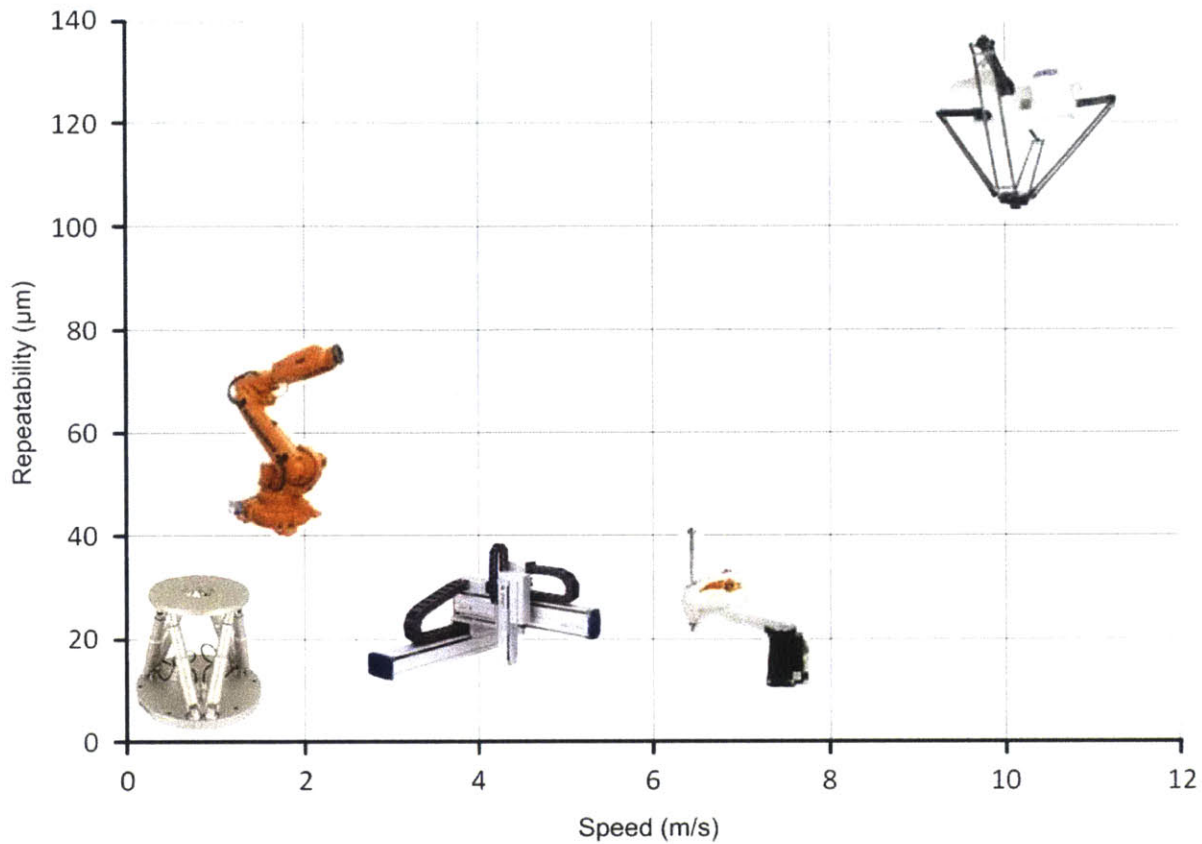


Figure 7: Approximate speed-repeatability relationship for various robot classifications. Comparing the range of values is difficult due to a lack of standardized tests and the variation of maximum speed at different points in the work volume due to robot geometry.^{60,62,96-98} Special thanks to my colleague Jamison Go for first assembling this data.

Given the high repeatability and low accuracy of most robot systems, significant effort has been invested in developing calibration techniques for improving robot accuracy. Error sources include geometric deviations; thermal expansion; and joint and link compliance.^{99,100} Controllers for most commercially available robotic systems are inaccessible to the end user for proprietary reasons, which complicates the calibration process. To overcome this limitation, calibration corrections are frequently performed via offline preprocessing, where the corrected joint angles are computed before being sent to the robot controller.⁹⁹ Existing literature catalogs many calibration techniques that have been developed.^{35,101-104}

OPPORTUNITIES FOR ROBOTICS IN ADDITIVE MANUFACTURING

Automation has been part of additive manufacturing since the beginning, when it was used to control the build platform of the stereolithography (SLA) printer made by Kodama in 1981.² Opportunities for new uses of robotics in additive manufacturing are increasing as robotics become more accessible and capable (precision, accuracy, load capability), and arguably are limited only by the imagination. This section explores recent applications of automation to additive manufacturing. Gantry and articulated arm systems have been adapted to industries ranging from manufacturing,¹⁰⁵ to shipping,¹⁰⁶ to material handling.¹⁰⁷ Technologies developed for these applications and others have been adapted to additive manufacturing by the addition of material deposition devices onto the system, in conjunction with the proliferation of inexpensive electronics and controls, which has reduced the cost of automation and system design.

Fused-deposition modeling (FDM) is currently expanding into the field of meter-scale objects, driven by the collaboration between Oak Ridge National Laboratory (ORNL) and Cincinnati Incorporated on a so-called big-area-additive manufacturing (BAAM) system.¹⁰⁸ The system is based on a commercial pellet extruder mounted to a large industrial gantry adapted from an industrial laser cutter.¹⁰⁹ Printing a car chassis was recently demonstrated in 44 hours.¹¹⁰ Figure 8 details the system and its capabilities.

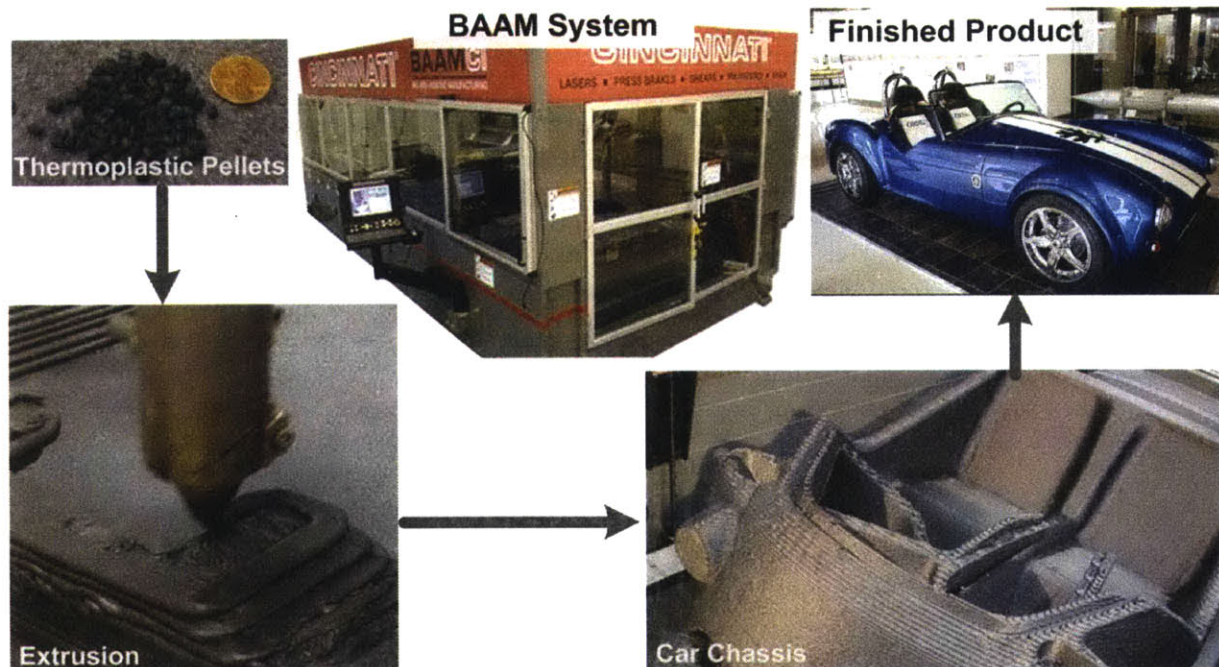


Figure 8: Big-area additive manufacturing of a sports car chassis using carbon-fiber filled thermoplastic and extrusive deposition.^{110,111}

The company Viridis3D has created an additive manufacturing system for creating sand casting molds via binder jetting. The process uses an articulated robot arm to iteratively spread a layer of foundry sand and apply binder only where necessary to form the mold cavities.¹¹² The reconfigurable nature of the system lowers the cost of mold manufacturing and prototyping. See Figure 9.

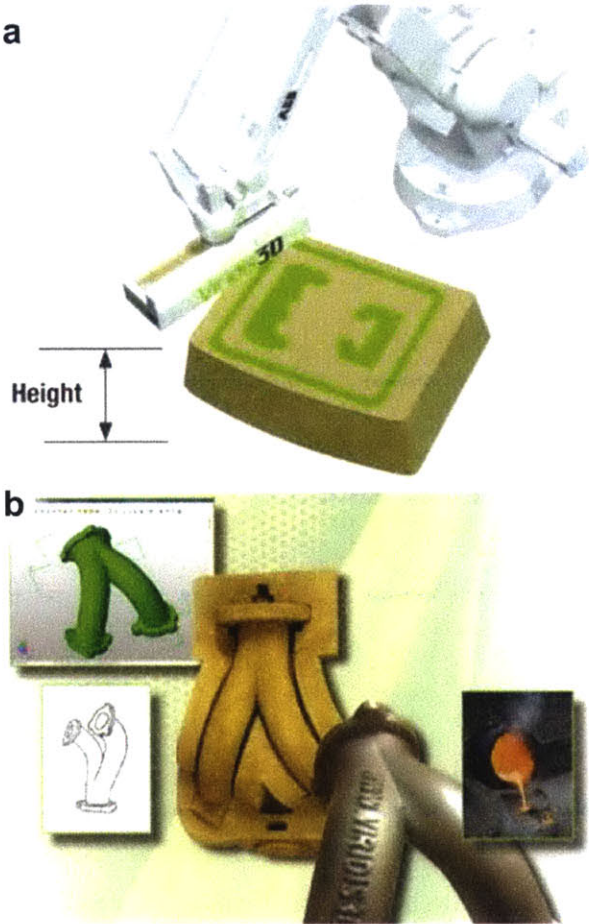


Figure 9: Viridis3D additive manufacturing of sand-casting molds using an articulated robot: a) The robot sweeps across the platform, depositing sand and selectively binding it;¹¹² b) After post-processing, the mold is ready for casting.¹¹³

Ford Motor Company has developed a technique for die-less single-point metal forming. While not strictly a demonstration of additive manufacturing, it is an excellent demonstration of automation systems applied to reconfigurable, digitally-driven manufacturing. The crux of the technology is a single point tool that iteratively deforms sheet metal until the final geometry is reached. To achieve this, a Cartesian gantry robot was coupled with custom software to generate the toolpath from a CAD file of the final part. The closed-loop gantry robot was selected since it's a high-stiffness design that can withstand the forces required to plastically deform the sheet metal. See Figure 10.

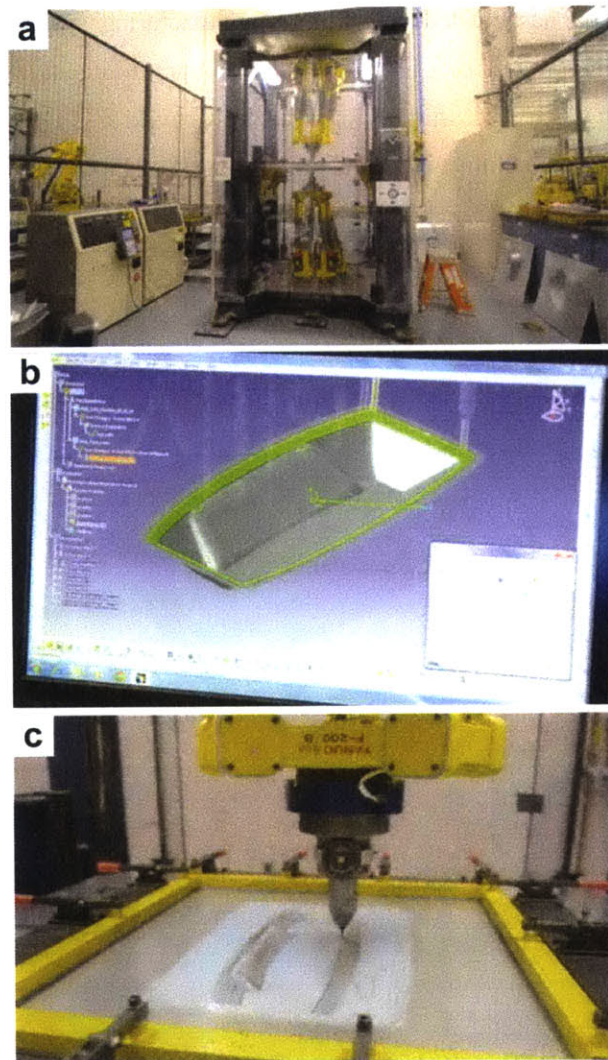


Figure 10: Ford single point sheet metal forming: a) System overview, showing the fixture and chassis; b) CAD interface showing the toolpath; c) Operation of the system showing the pointwise metal forming process.¹¹⁴

Construction and architecture is an environment traditionally dominated by manual labor, in spite of recent advances in robotics as applied to other fields.¹¹⁵ Extrusion methods for concrete, gypsum, sand, and stone powder have all been demonstrated,¹¹⁶ as well as several pick-and-place technologies for bricks.¹¹⁷⁻¹¹⁹

On a smaller scale, pick and place technology is an enabler for “voxelization” or “digital materials.” Digital materials are a class of materials that are deterministically assembled from smaller building blocks, each of which can contribute different functionality to the final part.¹²⁰ Digital materials allow for the assembly of final products with accuracy greater than the motion system performing the assembly. For

example, a child assembling LEGO bricks does not have the capability to position blocks with 5 micron accuracy, but due to the self-aligning nature of the blocks, the final product is more accurate than the system (child) used to manufacture the product.¹²¹ Digital additive manufacturing is still in the development stage, with only a few examples (with one process shown in Figure 11) using plastic and metal spheres¹²² as the building blocks.

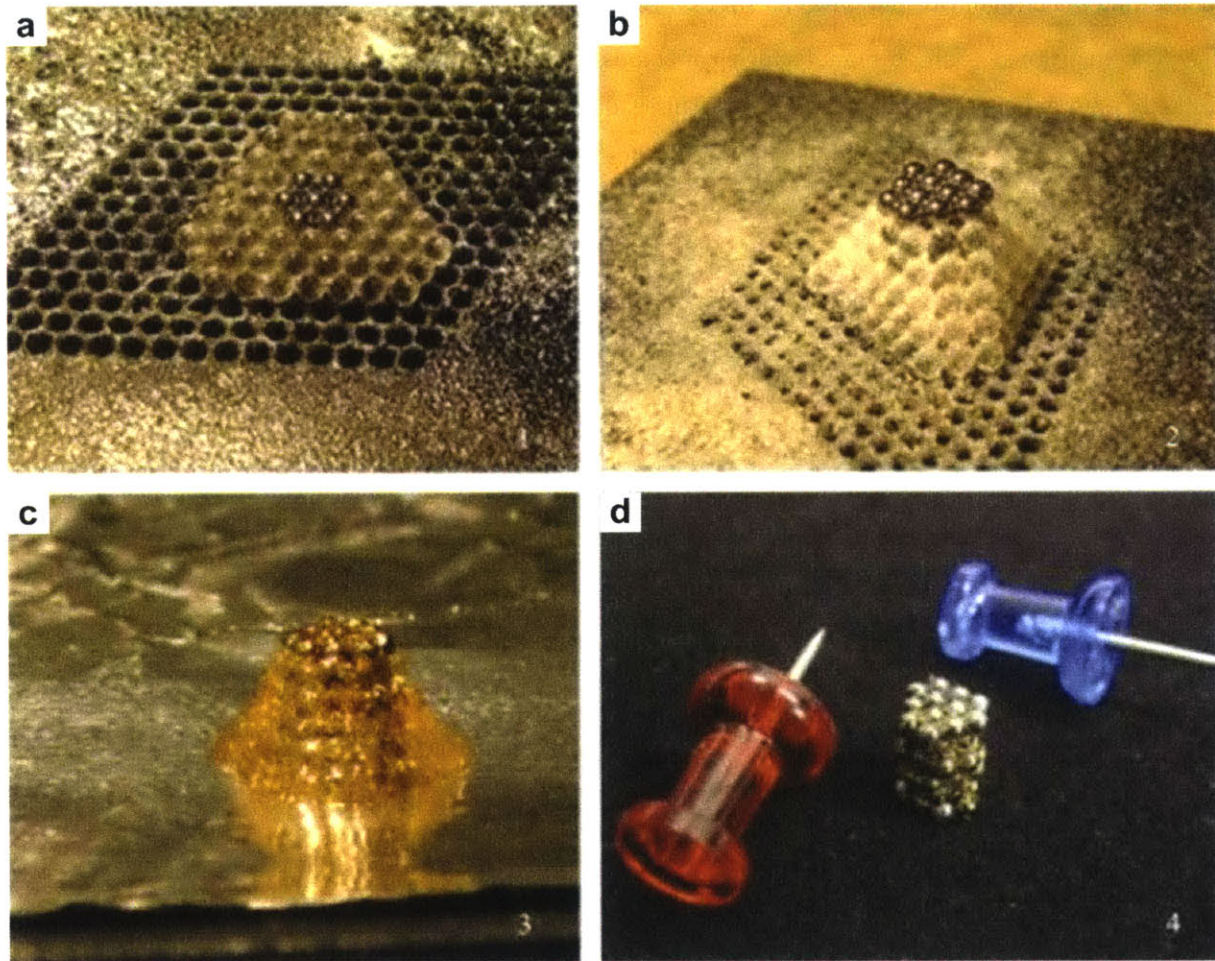


Figure 11: Example of voxel-based manufacturing using 1.5mm diameter spheres. Clear spheres are support material, steel spheres are structural material: a) Initial layer; b) Construction proceeds; c) Melting support material; d) Finished product, a simple column. Figure adapted.¹²¹

All of the processes discussed above would benefit from faster, more accurate, and/or stronger robots. Accuracy is especially important, as many applications require highly accurate systems that must be programmed offline.

CONCLUSIONS

According to Gibson et. al., there are four categories of systems used in additive manufacturing: liquid polymer systems, discrete particle systems, molten material systems, and solid sheet systems.¹²³ Gantry style systems are well suited to all of these methods since they are all fundamentally based on the concept of layered manufacturing, where a three-dimensional object is manufactured by iteratively depositing material in two-dimensional slices.

The traditional additive manufacturing methods described above do not pattern or build structures directly onto existing products and objects. This is due to the fact that the 3 axis gantry motion system is not well suited to patterning non planar substrates. Additional axes allow for the patterning of more complex geometries, with the 6-axis system the minimum number of axes required to have complete freedom of manipulation for an end effector. Appreciation of the performance and limits of robotic technology is essential to subsequent chapters, where I will present a design of a system for patterning on pre-existing objects using a six axis robot and rotary stage as the motion system.

intentionally blank

intentionally blank

Chapter 3: Design and Operation of a Robotic System for Photopatterning of Freeform Surfaces

This chapter describes the design and calibration of the maskless robotic lithography system. The system design was motivated by the myriad applications of micro-patterned planar surfaces, including directed cell growth and engineered wettability, which could enable new applications if extensible to freeform three-dimensional surfaces.

Therefore, I set out to design a fully automated system capable of patterning objects of complex curvature that fit in a 25cm-square bounding box (volume arbitrary, but chosen to enable a variety of demonstrations while using relatively compact motion systems). Requirements include 100 μ m positioning accuracy, 10 μ m projection resolution, development of a method for synchronizing a projection lithography system with multiple motion systems, and development of a method for digitally representing the surface of a 3D workpiece. This chapter describes the design, calibration, and operation of this system. This work began as my undergraduate mechanical engineering senior design project (part of the course ME450) while at the University of Michigan, mentored by Dr. Ryan Oliver.

SYSTEM DESIGN OVERVIEW

The system consists of three hardware modules connected and synchronized via software: 1) Maskless lithography end effector. 2) Robotic manipulator. 3) Rotary stage. This section describes the components in each subsystem and the design decisions used to select each. Figure 12 shows the system overview and Figure 13 contains a diagram of power and data flow.

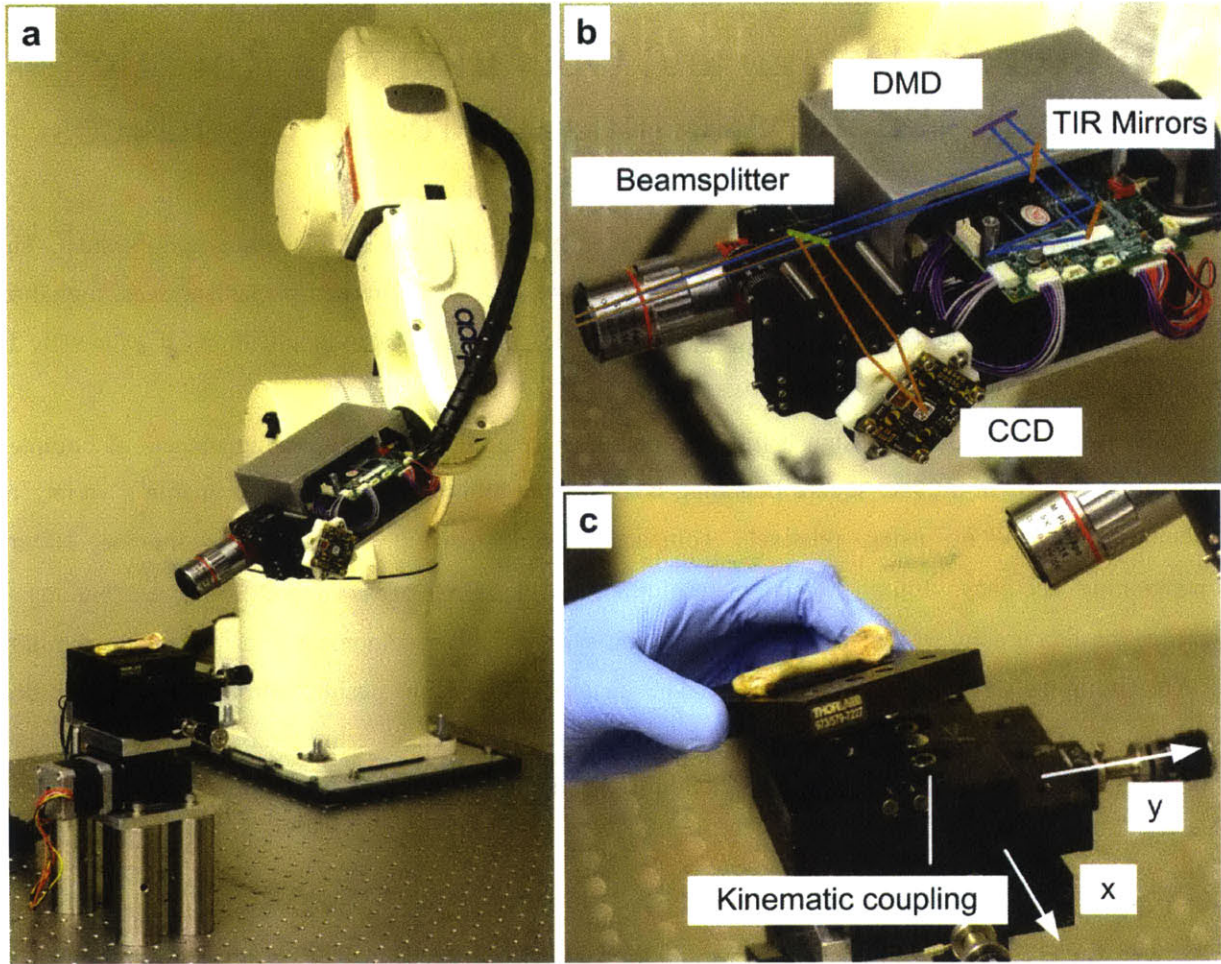


Figure 12: System overview. a) Motion systems; b) Projection lithography system built around digital micromirror device (DMD); c) Kinematic coupling for mounting workpiece in system.

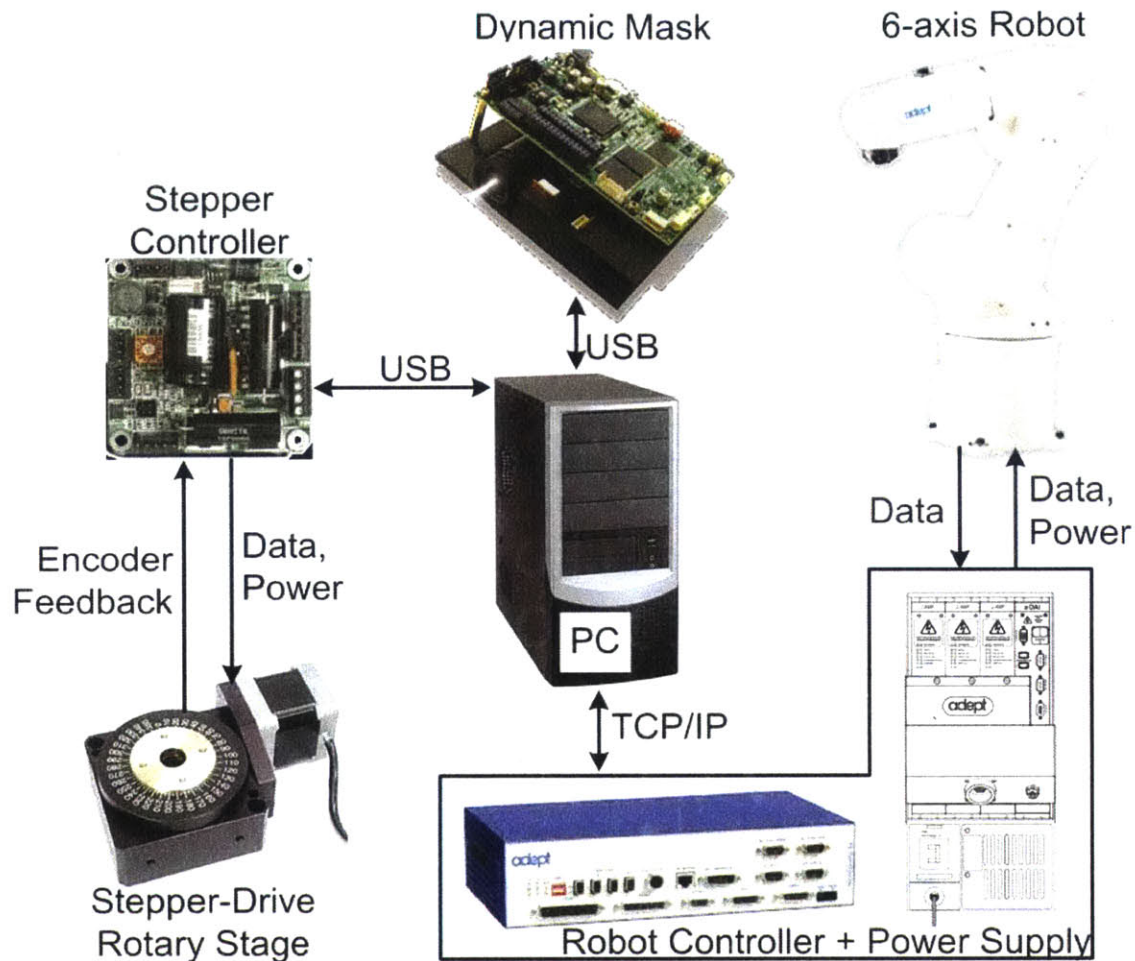


Figure 13: Diagram of power and data flow throughout the system. All actions are centrally controlled by the PC running custom software.¹²⁴⁻¹³⁰

The operational steps are: mounting the workpiece, 3D scanning the workpiece, depositing photoresist on its surface, preparing a texture file from the 3D scan output, and finally exposing sequentially over the entire part and developing the latent photoresist image. The procedure is outlined in Figure 14 and discussed in detail below.

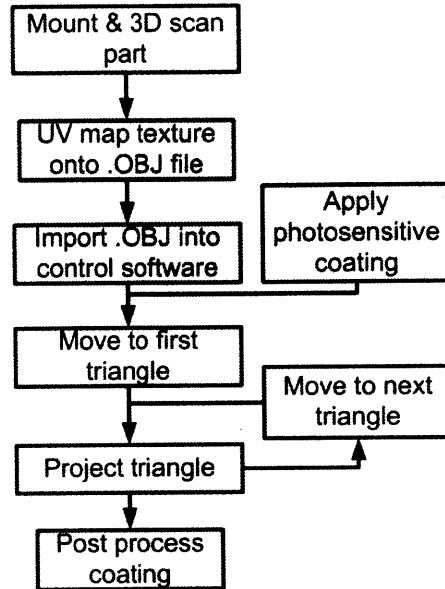


Figure 14: Outline of system operation steps.

Workpiece Fixturing

The workpiece is mounted to a kinematic coupling compatible with the coupling receptacle installed on the rotary stage. A kinematic coupling is a mechanism design for deterministic, repeatable fixturing based on precisely constraining an object in 6 dimensions (3 translational and 3 rotational) through the use of six point contacts. This exact constraint makes for a highly repeatable fixture, with designs frequently capable of 10-0.1 μ m repeatability.¹³¹ Workpiece mounting varies based on part geometry. After successful mounting, the part must be cleaned with acetone and isopropanol (or other solvents if solvent compatibility issues exist) and dried under an air stream in order to remove any residual dirt and oils.

3D Scanning Workpiece

Next, the workpiece, mounted on the upper kinematic coupling, is scanned using a commercially available NextEngine 3D laser scanner set to the highest resolution settings. This process takes anywhere from 1-2 hours. The result of the scan is a triangulated OBJ file containing a digital representation of the workpiece.

UV Mapping Digital Model

At this point, the OBJ file does not contain any information about the pattern to project for each triangle the end user wishes to apply to the workpiece. Using Blender, an open source graphics program, the mesh can be UV mapped with the desired texture. See below for a detailed discussion of UV mapping.

Exposure and Coordinated Motion

Exposure times depend on photoresist used. The optimum exposure times were determined experimentally. Once measured, the time in seconds is entered into the software as a global variable.

The intended pattern is exposed sequentially through coordinated motion of the robot and rotary stage, moving the projection lithography system antiparallel to the normal of each triangle.

Post-Processing

Photoresist development procedures vary based on photoresist. For the commonly used MicroSpray aerosol Novalok photoresist, the workpiece is immersed in 0.1N NaOH for 5 minutes with agitation.¹³² After 5 minutes the part is rinsed with DI water to remove residual resist. The final part is dried under nitrogen or dry air.

Poly (ethylene glycol) diacrylate photopolymer is developed by rinsing away the uncured resist using isopropanol and drying under nitrogen or dry air.

For both methods, characterization is performed via a combination of optical and scanning electron microscopy.

SYSTEM DETAILS

This section discusses the design of the system. Included is a discussion of the system control software and digital workpiece representation scheme, detailed design analysis of the hardware components, and error analysis of the positioning system.

Software

Coordinated motion and timing of each component is necessary to conformally pattern in three dimensions. This task is controlled by software implemented in C++.

Digital Workpiece Representation

In order to position the robot appropriately relative to the workpiece and display the proper mask at each location, the software must be given some description of the workpiece geometry and surface pattern. This description is provided by an OBJ geometry file, which was first developed by computer graphics company Wavefront Technologies and is now openly available. An OBJ file is a text file containing the vertices, faces, and texture coordinates necessary to describe a three-dimensional geometry in terms of a triangulated surface.

Vertex normals, vertex coordinates, vertex texture coordinates, and face descriptors are all stored in a list in the same OBJ file and indicated by unique letter(s) that begin each line. Vertex normal lines begin

with “vn,” vertex coordinate lines begin with “v,” vertex texture coordinate lines begin with “vt,” and face descriptor lines begin with “f.” The first line containing a vertex coordinate, regardless of where it appears in the file, is stored in computer memory as vertex coordinate 1, with the second appearing being vertex 2, etc. Vertex normals, vertex texture coordinates, and face descriptors follow the same numbering rule. Faces are described by three groupings of three numbers each, showing the vertices, texture vertices, and normal vertices associated with that face. The standard template is: “f v1/vt1/vn1 v2/vt2/vn2 v3/vt3/vn3.” Figure 15 shows a typical OBJ file and associated MTL file (which contains the texture data). The units in an OBJ file are arbitrary; it is up to the user to scale them appropriately.

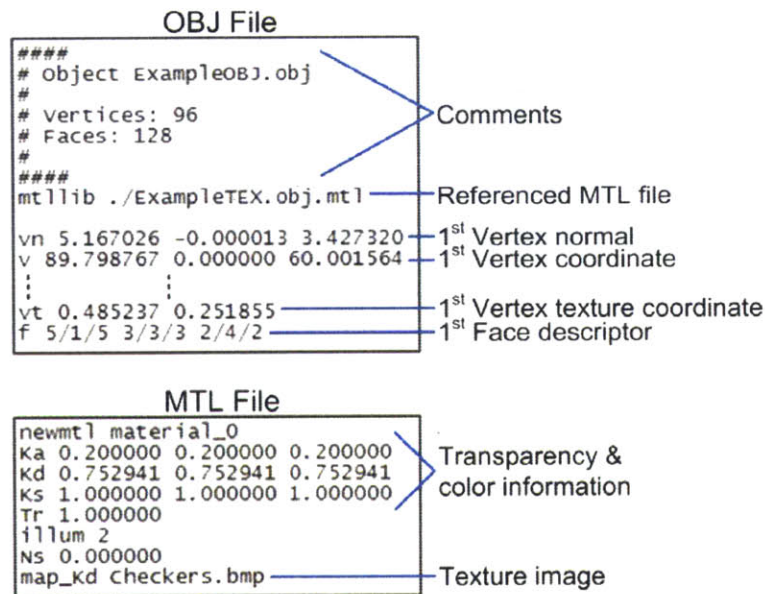


Figure 15: Annotated excerpts from an OBJ and MTL file pair. The OBJ file contains the vertex, texture, and face information for a given geometry, while the associated MTL file contains the link to the texture bitmap.

The triangular mesh defined in the OBJ file format described above is given a pattern through a technique known as UV mapping, which associates each triangle in the mesh with a subsection of a two-dimensional image (here, a bitmap, extension .BMP). When rendering the mesh, the subsection of the bitmap associated with each triangle is “painted on” that triangle in the mesh, giving the otherwise featureless mesh geometry a texture. Figure 16 shows the concepts behind UV mapping, starting with an unpatterned geometry, “unwrapping” that geometry onto a 2D image to associate each triangle with a texture, and then “rewrapping” the patterned triangles back into a 3D model. For more complex geometries, the mesh is first digitally sliced into multiple, simpler sub-meshes before patterning and rewrapping (i.e. for a rabbit, the mesh corresponding to the ears would be unwrapped and patterned separately from that of the body, etc.).

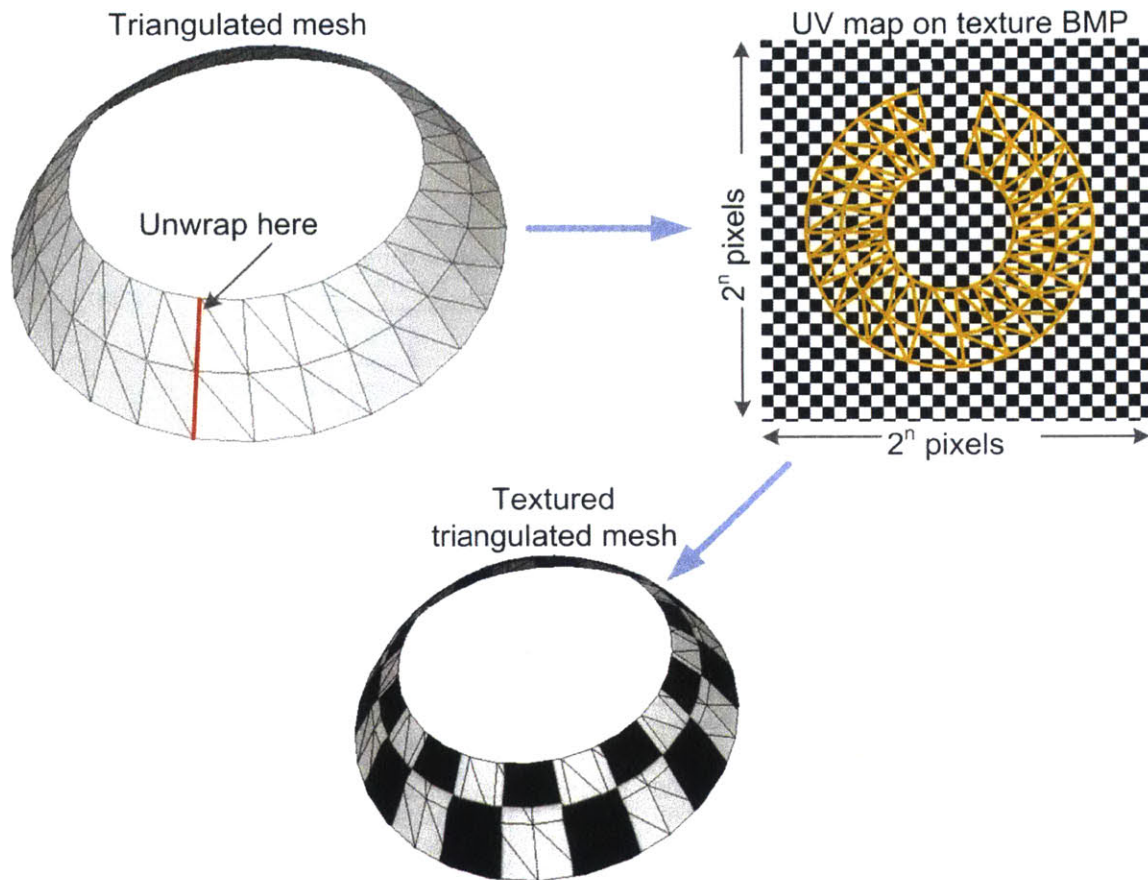


Figure 16: UV mapping overview: A digital model is “unwrapped” along a seam and the now-flattened mesh is associated with a digital image file (in this thesis, a BMP with the requirement of 2^n pixels per side, where $n < 14$ for memory reasons). Subsequently, the mesh is “rewrapped,” yielding a 3D digital model with an applied 2D texture. More complicated 3D models are sliced into simpler subsections before unwrapping and are recombined by reversing the slicing process after texturing (this is performed automatically by UV mapping software).

Software Overview

Figure 17 is a flowchart of the patterning algorithm. In summary, the algorithm translates the robot such that the surface normal of the i th triangle is antiparallel to and collinear with the ray exiting the center of the projection cone. At this point the projector changes from 600-700nm wavelengths (red) to 300-400nm (blue) and the intensity of blue light is increased to 0.6 or 1600 mW/cm², depending on the projection optical configuration in use. This completes exposure of the photoresist. The software then advances to the $(i+1)$ th triangle, sends commands to reposition the motion system, and the process repeats. The triangles are ordered in the OBJ file roughly by nearest neighbor, according to the open-source modeling software Meshlab.

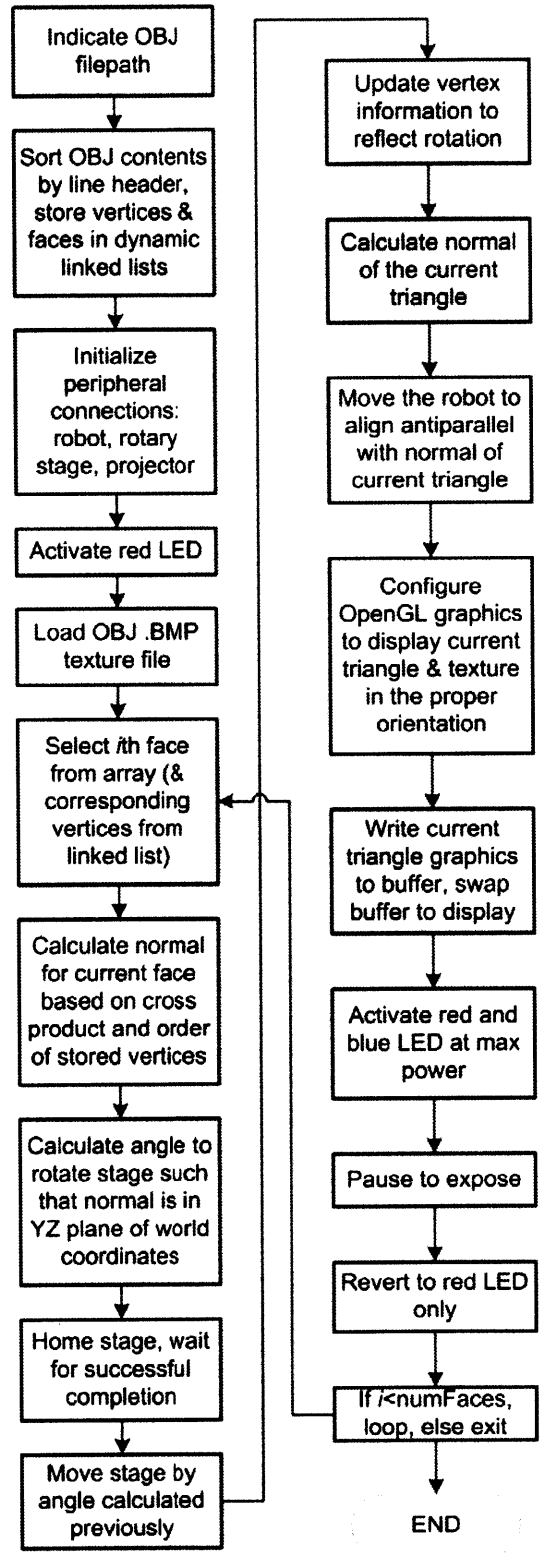


Figure 17: Process flow for the patterning software.

Hardware Module Design

This subsection discusses the design details and decisions used to select the components of the three hardware subsystems: 1) Maskless lithography end effector; 2) Robotic manipulator; 3) Rotary stage.

Maskless Lithography End-Effector

The projection lithography system uses a digital light processing (DLP)-based end effector. Digital light processing projectors are a specific form of digital micromirror device, which is in turn an example of a Micro-Opto-Electro-Mechanical System (MOEMS). The DLP technology was commercialized in 1996 by Texas Instruments.²⁷ Each DLP chip consists of over one million aluminum-coated micromirrors arrayed above a memory chip, one mirror per memory cell. The mirrors are electrostatically actuated by the charge stored in the memory bits.²⁷ DLP chips have been consistently increasing in array size, from 1280x1024 in 1998 to 2560x1600 in 2014.^{27,133} Since commercialization, DLP chips have found many applications, from pocket-sized pico-projectors to cinema-grade high-resolution systems consisting of one DLP chip for each primary color (red, green, and blue) with the final image consisting of a superposition of each micromirror array.^{134,135}

In the robotic lithography system, the optical end effector is based on the LightCrafter 4500 DLP development kit, a product designed to accommodate research and development of DLP applications. The LightCrafter 4500 is composed of a 912 x 1140 grid of square micromirrors that are 10.8 microns across the diagonal.¹³⁶ Since the projection system is used as-delivered, design of the optical train didn't need to be considered, but the layout will be discussed briefly here. The optical train consists of red, blue, and green LEDs with beams combined by dichroic mirrors before impinging on the DLP surface. The LEDs are digitally controlled via pulse-width modulation in order to create the illusion of a full spectrum of colors.

To ensure that the projection lithography system is capable of resolving individual micromirrors and therefore operating at the maximum possible resolution, the objective lens must be capable of resolving two neighboring mirrors in the DLP array. An optical system is considered capable of resolving two points if the Airy disks formed by each point are capable of being recognized as independent discs.¹³⁷ The Airy disk is the ringed appearance of a point source in a perfect lens with circular aperture due to diffraction limits from the wave nature of light.¹³⁸ Figure 18 shows an example Airy disk and the difference between resolved and unresolved points.

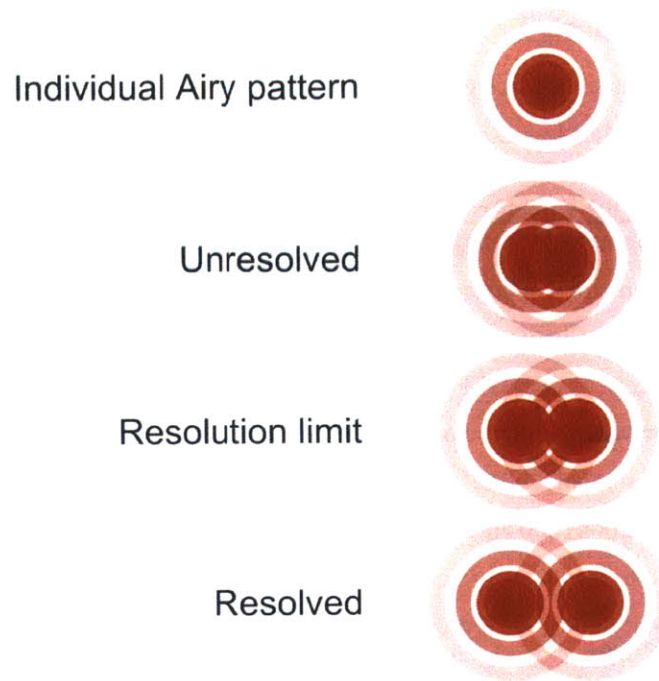


Figure 18: Example Airy disk and comparison of neighboring points in different states of resolution. Inspired by.¹³⁷

Knowing this, we want to calculate the smallest feature that can be resolved by the objective lens on the maskless lithography system. For a given wavelength and operating medium, resolving power is a function of the amount of light from a given point that the objective can collect--this quantity is called the numerical aperture (NA) and it accounts for the amount of light received by the optics (cone angle, α) and the index of refraction (n) of the working medium (Eq. 3 and Figure 19).¹³⁹

$$NA = n \sin(\alpha) \quad \text{Eq. 3}$$

For a microscope objective, the approximate relationship between resolution, r ; light wavelength, λ ; and numerical aperture, NA ; has been found to be:¹³⁷

$$r = \frac{\lambda}{2NA} \quad \text{Eq. 4}$$

Empirical observations by microscope manufacturers have led to the following relationship between magnification factor, M , and numerical aperture:¹⁴⁰

$$M = 500 \text{ to } 1000 \cdot (NA) \quad \text{Eq. 5}$$

The magnification factor is provided as a range of values, since the exact value will depend on the presence or absence of other optical elements in the system. Since magnification is a simple scale factor, it follows that the size of an individual pixel image when projected on the workpiece is described by Eq.

6, where $10.8\mu\text{m}$ is the diagonal measurement of a physical micromirror. Note that the magnification factor is the divisor, since the image formed is *smaller* than the object.

$$P_i = \frac{10.8 \mu\text{m}}{M} \quad \text{Eq. 6}$$

The above equations describe the performance characteristics of the objective-lens projection lithography system. From Eq. 3 and Eq. 4, an estimate for the smallest resolvable feature is found to be approximately $1\mu\text{m}$, based on a calculated numerical aperture of 0.2 and an operating wavelength of 400nm . Therefore, the optics can successfully resolve neighboring $10.8\mu\text{m}$ pixels on the DMD. The size of the image formed on the workpiece surface from an individual micromirror on the DMD is calculated from Eq. 5 and Eq. 6 and found to be between 50 to 100nm , which indicates the approximation in Eq. 5 is not valid, likely due to the deviation in the projection system design from a standard microscope (for which the equation was originally applied).

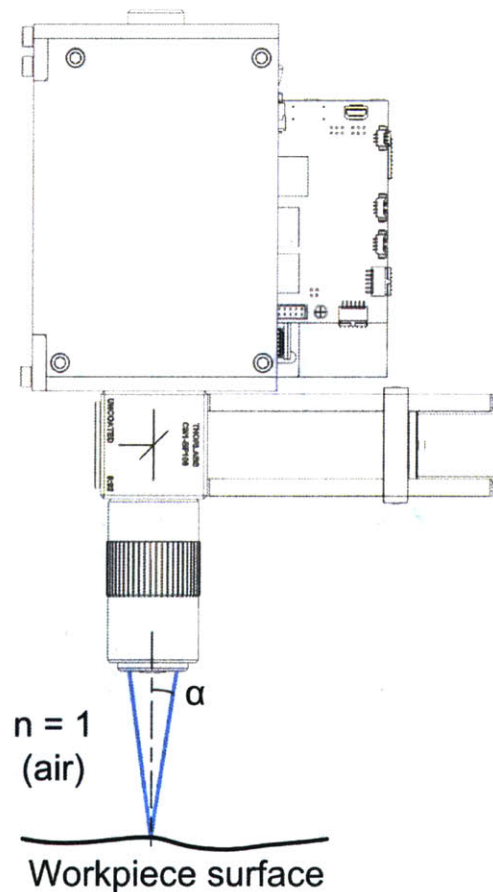


Figure 19: Cone angle, α , of projection system for calculation of numerical aperture. The index of refraction of the working medium is described by the variable n .

For the given optical system, power flux is a function of field of view (FOV), since the LEDs can provide a given maximum power independent of the magnification used. Higher magnification will result in a smaller field of view and correspondingly higher power flux (mW/cm^2), at the expense of exposure area.

Two variants of the projection lithography end effector have been developed for this system. The first is based around the as-delivered optics on the LightCrafter 4500. In this configuration, the optics magnify the DLP array, projecting a 144.2 by 227.0mm image at a focal distance of 472.1mm (as measured). The size of an individual mirror at this magnification is $220\mu\text{m}$ on the diagonal, as measured by optical microscopy. For this variant, the power flux at the workpiece surface was measured to be $0.6 \text{ mW}/\text{cm}^2$.

The projection unit is mounted to an optical breadboard with toe clamps and the breadboard is bolted onto the robot end effector using the standard end-effector mounting pattern. The lack of alignment devices introduces uncertainty with the location of the projection system relative to the workpiece, but the calibration procedures discussed below account for this. In addition, the large field of view makes it more forgiving to robot accuracy errors, as a given error is only a small fraction of the pattern projected. Figure 20 shows the layout and light path in this projection system.

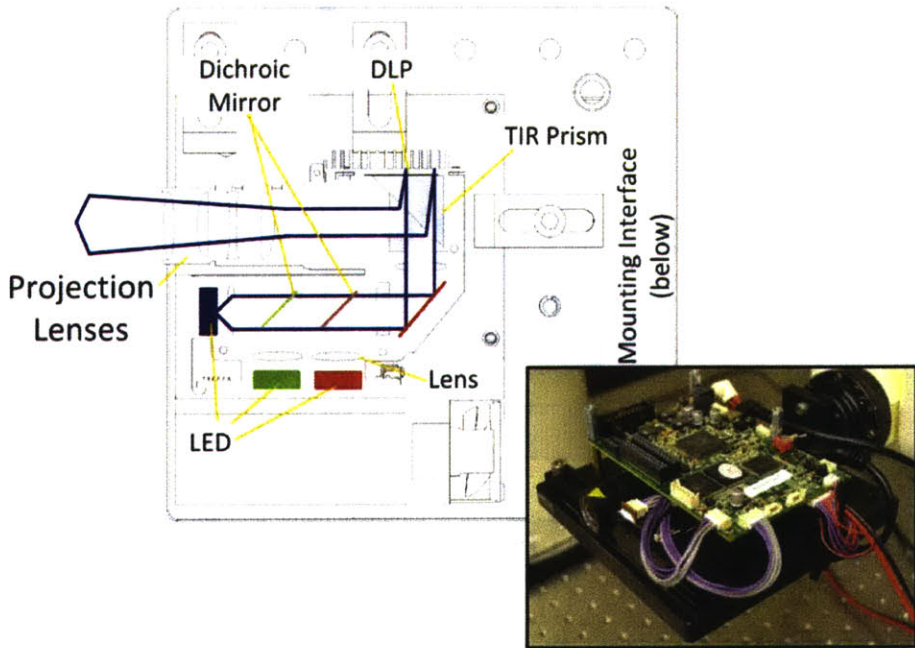


Figure 20: Cutaway view of wide-angle projection lithography end effector. The projector is mounted on a breadboard via toe clamps and the assembly is bolted to the robot end effector using a right-angle mount. The commercially-supplied projection lens is used to expose a large area on the workpiece. Inset shows system mounted on end effector.

The second end effector design incorporates the LightCrafter 4500 control circuitry and DLP chip into a custom-built aluminum enclosure. The enclosure supports a 5x microscope objective mounted on a 90:10 Pellicle beamsplitter. The beamsplitter is oriented such that 90% of the projection light passes to the substrate and 10% of the return light is passed to the coaxial CCD. Incident light on the CCD is further filtered by a longpass filter. This allows imaging in red light while simultaneously exposing in blue light, all while avoiding CCD saturation. See Figure 21.

For each end effector, patterning rate is a function of the periodic projection area, A [cm^2/cycle] and cycle frequency, F [1/s], which is itself the sum of exposure time t_E and repositioning time t_R (Eq. 7).

$$F = \frac{1}{t_E} + \frac{1}{t_R} \quad \text{Eq. 7}$$

Subsequently, the end effector patterning rate, R [cm^2/s] is

$$R = AF \quad \text{Eq. 8}$$

Using the exposure areas tabulated in Table 1 in conjunction with exposure times from Chapter 4 (2 seconds and 7 minutes for the microscope objective and projection lens end effectors, respectively) and repositioning time from Chapter 4 (2 minutes), the patterning rate is calculated for each end effector and reported in Table 1.

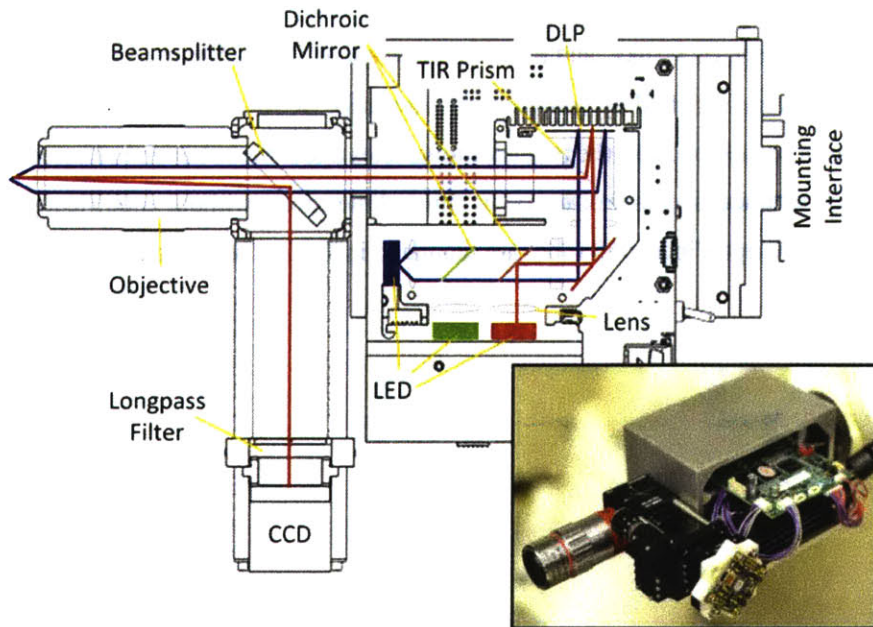


Figure 21: Cutaway view of the objective optics end effector, which incorporates a custom aluminum enclosure. The beamsplitter allows the CCD to image the surface of the workpiece while the LEDs simultaneously cure the photoresist. The objective lens reduces field of view but significantly increases light intensity, even though some light is lost due to absorption in the additional lenses. Inset shows system mounted on end effector.

Table 1: Comparison of microscope objective and projection lens end-effectors.

Optical Characteristics	Microscope	
	Objective	Projection Lens
Min. Feature Size (μm)	10	220
Max. Exposure Area (cm^2)	0.12	327
Power Areal Density (mW/cm^2)	1600	0.6
Working Distance (cm)	28.4	42.7
Max. Patterning Rate (cm^2/s)	0.06	3.5

Robotic Manipulator

The motion system consists of a six-axis articulated robot (Adept Viper s650) combined with a stepper motor-driven rotary stage (Velmex B5990TS). Both are mounted onto a custom-built isolation table with an optical breadboard. The goal of the positioning system is to accurately and precisely focus the projection from the maskless lithography system normal to the substrate at the correct focal distance. The rotary stage is mounted on a 12.5 mm thick aluminum plate that is spaced from the optical table using four 100 mm optical posts (Thorlabs P4) which have a length tolerance of ± 0.127 mm.

Selection of a six-axis articulated robot as the prime motion system was based on a capability comparison of existing commercial robots. System repeatability was desired to be in the range of 15-30 μm , payload in the range of 3-10kg, and reach in the range of 500-1250mm. As demonstrated by Figure 22, these requirements are satisfied by commercially available SCARA and articulated robots. A six-axis articulated robot was chosen because the two additional axes allow the robot end effector to pitch and roll, enabling the robot to trace a complex curve in three dimensions without modification. Manufacturer specifications for the Adept Viper s650 robot are tabulated in Table 2 and Table 3.

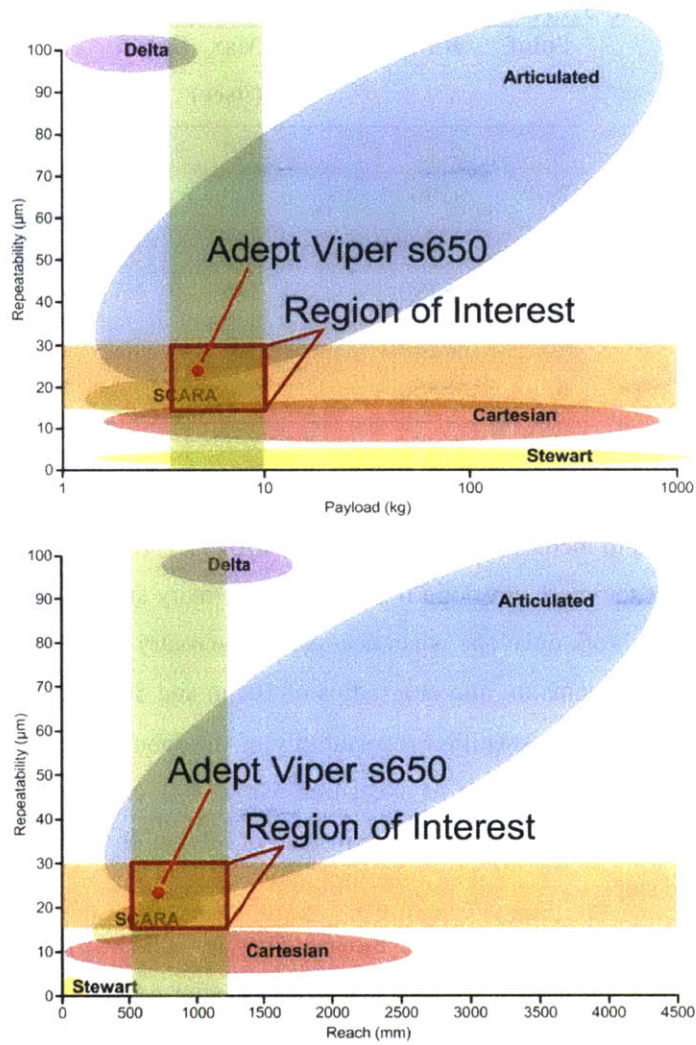


Figure 22: Robot selection charts (adapted from Ch. 2) showing the regions of interest based on the system requirements and the suitability of the Adept s650.

Table 2: Adept Viper s650 manufacturer specifications.¹⁴¹

Parameter	Value
Reach	653mm
Payload	5kg
Repeatability	$\pm 0.020\text{mm}$
Mass	28kg

Table 3: Adept Viper s650 joint ranges and speeds.¹⁴¹

Joint	Range (°)	Max. Speed (°/sec)
1	±170	328
2	-190 to +45	300
3	-29 to +256	375
4	±190	375
5	±120	375
6	±360	600

Rotary Stage

The rotary stage is used to increase the maximum part size that can be patterned. For example, a large part need only fit into half the work envelope if mounted on a rotary stage, as the stage can be rotated to bring the other half into the work envelope when necessary. The rotary stage introduces an accuracy error of 100 arc-seconds, which amounts to 5 μ m at a radius of 10mm and 50 μ m at 100mm from the center of rotation. This is comparable to the specified repeatability of the robot. The rotary stage is driven by a stepper motor, but angular displacement is measured via a 400 count-per-revolution encoder with quadrature, giving 1600 CPR. The encoder is used instead of relying on open-loop stepping to eliminate the possibility of skipped steps.

The workpiece is mounted on a kinematic mount (Thorlabs KB3X3) (Figure 23). This allows for rapid, repeatable workpiece positioning in the work envelope after scanning and photopolymer coating. Positioning errors are minimized (to within the repeatability of the kinematic mount—30 μ m) since the workpiece is indexed relative to the kinematic mount (as described above), so repeatable location of the kinematic mount on the kinematic coupling results in repeatable placement of the workpiece in the robot work envelope. The kinematic mount is attached to the rotary stage using a custom adapter plate made of aluminum. Two orthogonal micrometer stages (Thorlabs PT1A) are mounted between the kinematic mount and the rotary stage in order to remove runout (discussed in detail in System Calibration section). In standard operation, the runout of the rotary stage can be reduced to $\pm 12\mu$ m.

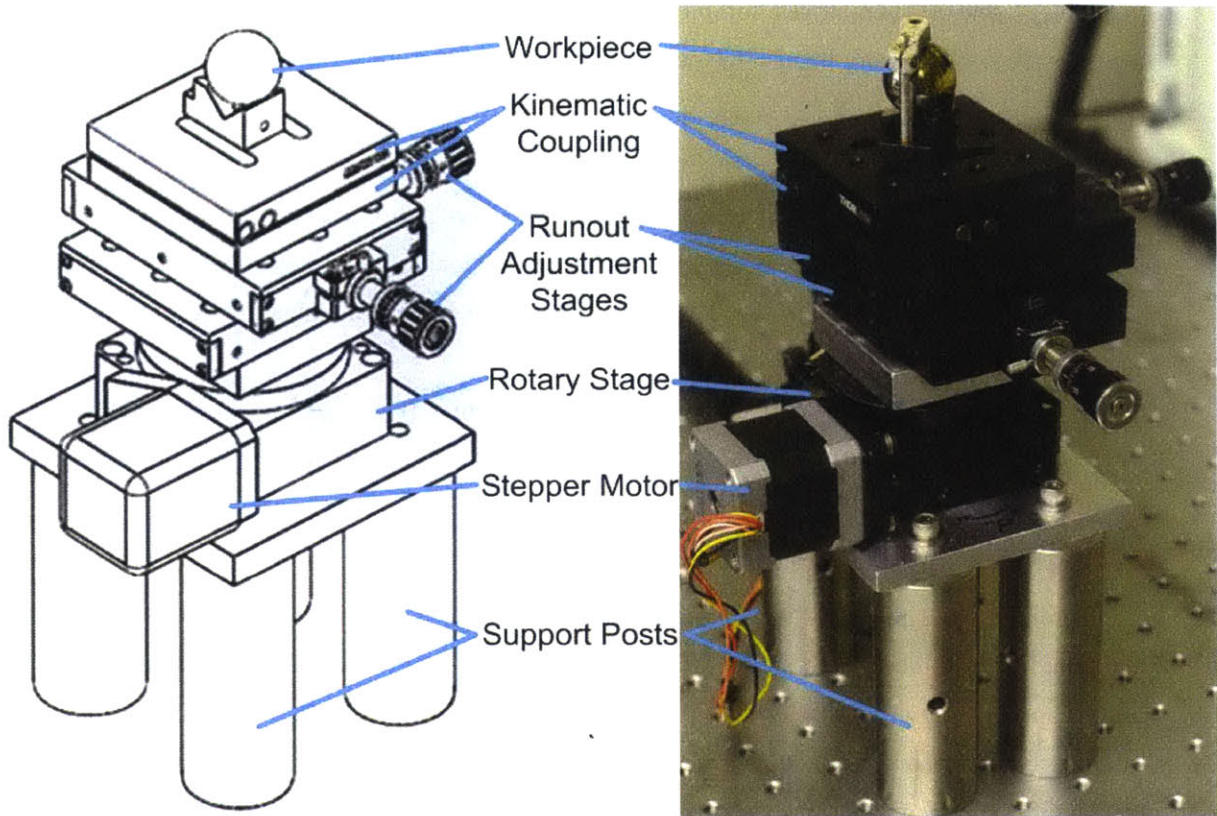


Figure 23: Rotary stage configuration, with key components labeled. The workpiece shown here is a 25.4mm diameter stainless steel sphere.

Modeling Motion System Error

To understand the positioning performance of the system we first develop a mathematical model using kinematics and closed structural loops. This model is based on a serial chain of rotary elements, whose relative position and orientation are known. This allows the systematic introduction of position and orientation errors to the linkage elements to understand which system components contribute the most overall error and how they may be improved or controlled.

The analysis was performed with the robot in a specific arbitrary position (shown in Figure 12a) during exposure. In this pose, the robot was modeled as a serial linkage using homogeneous transform matrices, where the orientation and position of each joint is described mathematically relative to the previous joint. The prototypical HTM is shown in Eq. 9.

$$H_i^{i-1} = \begin{bmatrix} R_{i3 \times 3} & P_{i3 \times 1} \\ 0_{i1 \times 3} & 1 \end{bmatrix} \quad \text{Eq. 9}$$

The nomenclature H_i^{i-1} indicates that this HTM describes the position of joint i in the coordinate system of joint $i - 1$. The HTM is composed of $R_{i3 \times 3}$, a 3x3 rotation matrix; $P_{i3 \times 1}$, a 3x1 translation vector; $0_{i1 \times 3}$, a 1x3 vector of zeros (for bookkeeping); and 1, a 1x1 scalar. Computer graphics makes use

of the $0_{i1 \times 3}$ and 1 submatrices for modifying image perspective and scale, respectively, but these properties are not necessary in machine design and therefore the submatrices are held constant.⁴⁸

When filling out Eq. 9 for a given joint and link, the matrix is populated as follows. The translation from end $i - 1$ to end i of a given link is entered into $P_{i3 \times 1}$ submatrix, here comprised of scalar components a , b , and c . The rotational difference between the coordinate frames at $i - 1$ and i is accounted for in the $R_{i3 \times 3}$ submatrix, which can be rotation about a single axis or a combination of rotations, but care must be taken with the order of operations when combining multiple rotations. Here the example given is for rotation about the +Z axis:

$$H_i^{i-1} = \begin{bmatrix} \cos \theta_Z & -\sin \theta_Z & 0 & a \\ \sin \theta_Z & \cos \theta_Z & 0 & b \\ 0 & 0 & 1 & c \\ 0 & 0 & 0 & 1 \end{bmatrix} \quad \text{Eq. 10}$$

This procedure is then repeated for every link in the system.

Figure 24 shows the link-local coordinate frames used to generate the HTMs for the entire system. Each coordinate frame is described relative to the previous coordinate frame, starting from the triangle centroid and moving clockwise around the figure. Table 4 contains the displacement vectors to translate from coordinate frame $i - 1$ to coordinate frame i . The displacement values were used from the manufacturer-supplied robot link dimensions and direct measurements of the system for all other values. The local coordinate frames were set up such that there is no relative rotation in order to simplify the analysis. The individual matrices containing the displacement vector data are shown in Eq. 11-Eq. 21. The entire complex kinematic chain is represented as a sequential product of the individual homogeneous transform matrices and is shown in Eq. 22. Note that the displacement vector for the T matrix is zero, this is expected, since the system is a closed loop.

To identify the most sensitive linkage members, the system model was then analyzed using a perturbation analysis, which consists of making small fractional adjustments to link length and orientation and recording the resultant displacement at the end effector. Each link is given a length error of approximately $200\mu\text{m}$ and each joint an angular error of approximately 0.03° , which corresponds with 1-2 counts on a typical encoder.

The results of the perturbation analysis are shown in Figure 25. The joints of the articulated robot were found to dominate the positioning error of the system, with the individual joint that contributes the most error being joint 1--the first joint in the serial chain of the robot. This is explained by the fact that this first joint is furthest from the end effector, and therefore the sine error introduced by a given angular error has the furthest distance to propagate. This observation explains why larger articulated robots are

associated with larger repeatability errors—the cantilevered serial links readily magnify angular error across the robot.

Increasing absolute positioning repeatability is only possible by increasing the angular accuracy of the joint actuators, either through further calibration or the addition of machine-vision based positioning feedback. However, this analysis suggests that since the expected error is approximately $650\mu\text{m}$, each triangle should be much larger than $650\mu\text{m}$ in order for the positioning error to not dominate the pattern. In the next chapter, a demonstration of patterning triangles with 30mm legs is shown. At this relatively large length scale, a $650\mu\text{m}$ positioning error is approximately 2% of the triangle size and misalignment is not observable. Finally, note that the size of workpiece plays no role in the expected positioning error, as the error comes from the intrinsic properties of the robot joint encoders.

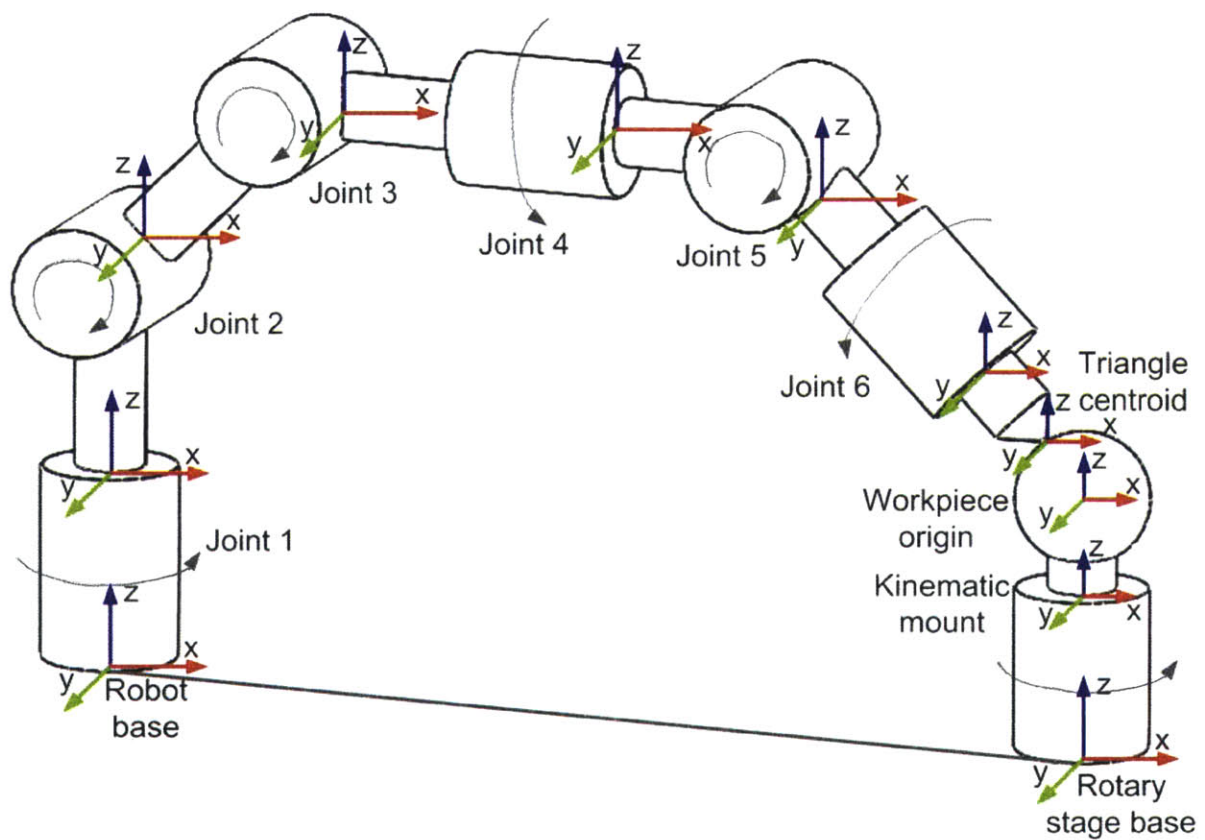


Figure 24: System linkage schematic used to define the homogeneous transform matrices. Joints are labelled to correspond with the error sources listed in Figure 25.

Table 4: HTM Parameters for 7-axis system

Axis number	Description	Relative Position from $i-1$ (mm)		
		X	Y	Z
0	Triangle centroid	0	0	0
1	Workpiece origin	10.46	1.86	-7.06
2	Kinematic mount	0	0.89	-36.66
3	Rotary stage base	0	0	-198.20
4	Robot base	-434.00	-445.20	0
5	Joint 1	0	0	197.70
6	Joint 2	24.05	89.54	148.00
7	Joint 3	-21.05	30.54	266.30
8	Joint 4	84.73	108.82	-7.06
9	Joint 5	53.74	140.57	-143.40
10	Joint 6	53.20	4.22	-54.67
11	Projection lightpath	228.80	68.80	-165.00

$$H_1^0 = \begin{bmatrix} 1 & 0 & 0 & 10.46 \\ 0 & 1 & 0 & 1.86 \\ 0 & 0 & 1 & -7.06 \\ 0 & 0 & 0 & 1 \end{bmatrix} \quad \text{Eq. 11}$$

$$H_2^1 = \begin{bmatrix} 1 & 0 & 0 & 0 \\ 0 & 1 & 0 & 0.89 \\ 0 & 0 & 1 & -36.66 \\ 0 & 0 & 0 & 1 \end{bmatrix} \quad \text{Eq. 12}$$

$$H_3^2 = \begin{bmatrix} 1 & 0 & 0 & 0 \\ 0 & 1 & 0 & 0 \\ 0 & 0 & 1 & -198.20 \\ 0 & 0 & 0 & 1 \end{bmatrix} \quad \text{Eq. 13}$$

$$H_4^3 = \begin{bmatrix} 1 & 0 & 0 & -434.00 \\ 0 & 1 & 0 & -445.20 \\ 0 & 0 & 1 & 0 \\ 0 & 0 & 0 & 1 \end{bmatrix} \quad \text{Eq. 14}$$

$$H_5^4 = \begin{bmatrix} 1 & 0 & 0 & 0 \\ 0 & 1 & 0 & 0 \\ 0 & 0 & 1 & 197.70 \\ 0 & 0 & 0 & 1 \end{bmatrix} \quad \text{Eq. 15}$$

$$H_6^5 = \begin{bmatrix} 1 & 0 & 0 & 24.05 \\ 0 & 1 & 0 & 89.54 \\ 0 & 0 & 1 & 148.00 \\ 0 & 0 & 0 & 1 \end{bmatrix} \quad \text{Eq. 16}$$

$$H_7^6 = \begin{bmatrix} 1 & 0 & 0 & -21.05 \\ 0 & 1 & 0 & 30.54 \\ 0 & 0 & 1 & 266.30 \\ 0 & 0 & 0 & 1 \end{bmatrix} \quad \text{Eq. 17}$$

$$H_8^7 = \begin{bmatrix} 1 & 0 & 0 & 84.73 \\ 0 & 1 & 0 & 108.82 \\ 0 & 0 & 1 & -7.06 \\ 0 & 0 & 0 & 1 \end{bmatrix} \quad \text{Eq. 18}$$

$$H_9^8 = \begin{bmatrix} 1 & 0 & 0 & 53.74 \\ 0 & 1 & 0 & 140.57 \\ 0 & 0 & 1 & -143.40 \\ 0 & 0 & 0 & 1 \end{bmatrix} \quad \text{Eq. 19}$$

$$H_{10}^9 = \begin{bmatrix} 1 & 0 & 0 & 53.20 \\ 0 & 1 & 0 & 4.22 \\ 0 & 0 & 1 & -54.67 \\ 0 & 0 & 0 & 1 \end{bmatrix} \quad \text{Eq. 20}$$

$$H_{11}^{10} = \begin{bmatrix} 1 & 0 & 0 & 228.80 \\ 0 & 1 & 0 & 68.80 \\ 0 & 0 & 1 & -165.00 \\ 0 & 0 & 0 & 1 \end{bmatrix} \quad \text{Eq. 21}$$

$$T = \prod_0^{11} H_i^{i-1} = \begin{bmatrix} 1 & 0 & 0 & 0 \\ 0 & 1 & 0 & 0 \\ 0 & 0 & 1 & 0 \\ 0 & 0 & 0 & 1 \end{bmatrix} \quad \text{Eq. 22}$$

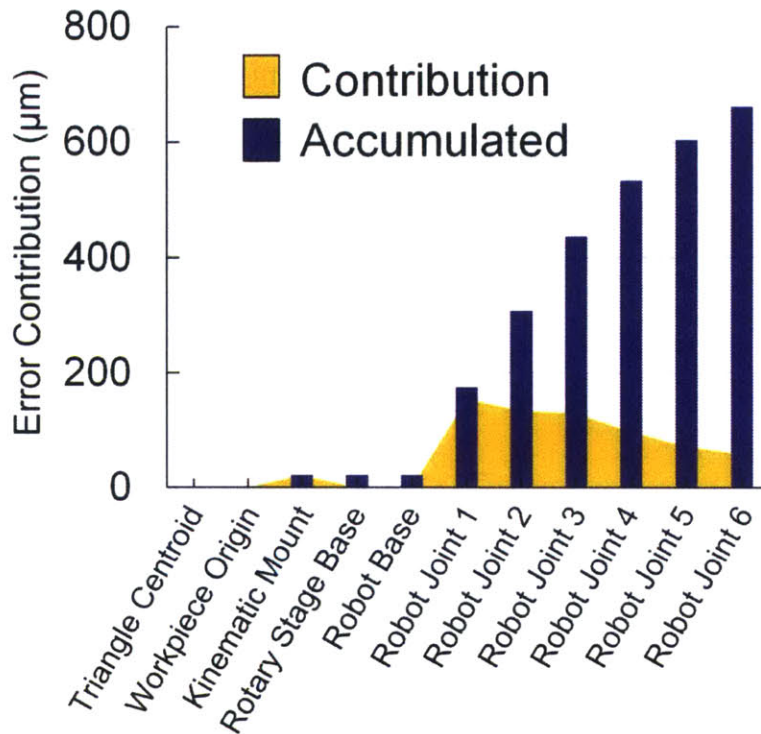


Figure 25: End-effector positioning error due to each system component. The first five items listed are static translation offsets and therefore don't contribute significantly to the error of the end effector once properly quantified. The robot joints dominate, as they are sources of sine error.

SYSTEM CALIBRATION

After system assembly but before operation, the system must be calibrated. The goal of calibration is to measure all static offsets in the system in order to properly account for them in software. Measurement is performed via a variety of techniques, including robot coordinate feedback and manual measurement with digital calipers.

Seven static offsets must be measured and entered manually into the software as global variables. The variable names are: ObjectX, ObjectY, ObjectZ, RobotOffset, XBarrelOffset, YBarrelOffset, and Roll. During calibration, the variables are measured in the order described here. Tabulated values for all the calibration constants are shared in Table 5.

ObjectX, ObjectY, and ObjectZ

These variables describe the world X, Y, and Z coordinates of the workpiece OBJ file origin (in millimeters). Measuring these variables is done using the position-query function of the robot arm. For example, to measure ObjectX, the robot is manually positioned via the teach pendant until the rotary stage

axis of rotation is visible in the center of the CCD when viewed from the +Y direction. Then the world coordinates of the end effector are queried and the X coordinate is recorded as ObjectX. A similar procedure is used to determine ObjectY and ObjectZ. Figure 26 shows the ObjectX, Y, and Z offsets relative to the world coordinate frame.

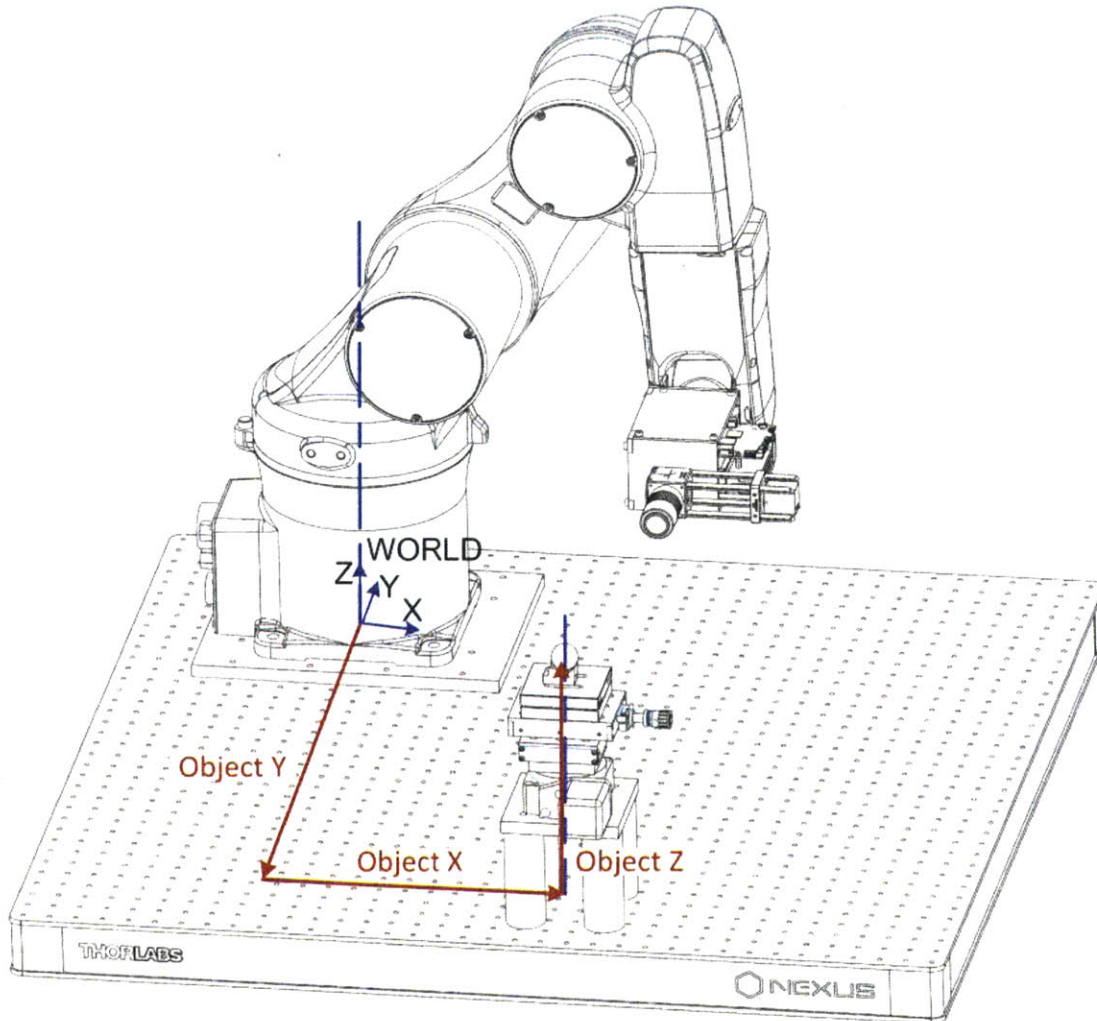


Figure 26: The location of the workpiece origin in world coordinates is described by a vector composed of ObjectX, ObjectY, and ObjectZ scalars.

RobotOffset

The distance between the robot end effector faceplate and the focal plane of the projection is stored in software as RobotOffset (in millimeters). This variable is a function of the physical size of the optics package as well as the focus distance (see Figure 27). The magnitude is calculated by focusing the projection on the table that the robot is mounted on and querying the robot end effector Z position. To

account for the thickness of the robot base plate, the base plate thickness of 12.7mm is then subtracted from the measured value to arrive at RobotOffset.

Roll

The Roll variable describes the degrees of rotation about the tool Z axis necessary to register the projected triangles with the workpiece, which is equivalent to aligning the bottom extent of the projection frame parallel to the world XY plane. The Roll angle is measured by reading the encoder values from robot joint 6 after manually registering the triangles using the teach pendant.

XBarrelOffset and YBarrelOffset

The barrel offset is the offset in the tool XY coordinate plane of the center of the projection relative to the center axis of the robot end effector, in millimeters. This is present due to manufacturing variation in the optics end effector. The primary source of this offset is the DLP chip mounting location in the projector, since the DLP chip location is not precisely defined. The displacement is described in the robot tool X Y coordinate frame by the variables XBarrelOffset and YBarrelOffset, respectively. Figure 27 defines the offsets.

To measure these offsets, the projection image is focused on a horizontal 50 μ m-square checkerboard pattern of known checker dimension and joint 6 is instructed to rotate in approximately 60° increments, with a photograph taken after each interval. In the resulting image sequence, the center of the projection can then be seen to orbit a fixed location, which is the axis of rotation of the end effector. The magnitude of the BarrelOffset vector is the radius of this circle. The vector components are then determined with knowledge of the roll angle measured previously:

$$XBarrelOffset = |BarrelOffset| \cdot \cos(Roll) \quad \text{Eq. 23}$$

$$YBarrelOffset = |BarrelOffset| \cdot \sin(Roll) \quad \text{Eq. 24}$$

Table 5: Measured values for the system calibration parameters. These are input into the software to register the workpiece relative to the robot world coordinate frame.

Offset	Value	Unit
ObjectX	338.926	mm
ObjectY	-412.00	mm
ObjectZ	217.060	mm
RobotOffset	472.123	mm
Roll	3.413	°
XBarrelOffset	79.858	mm
YBarrelOffset	4.763	mm

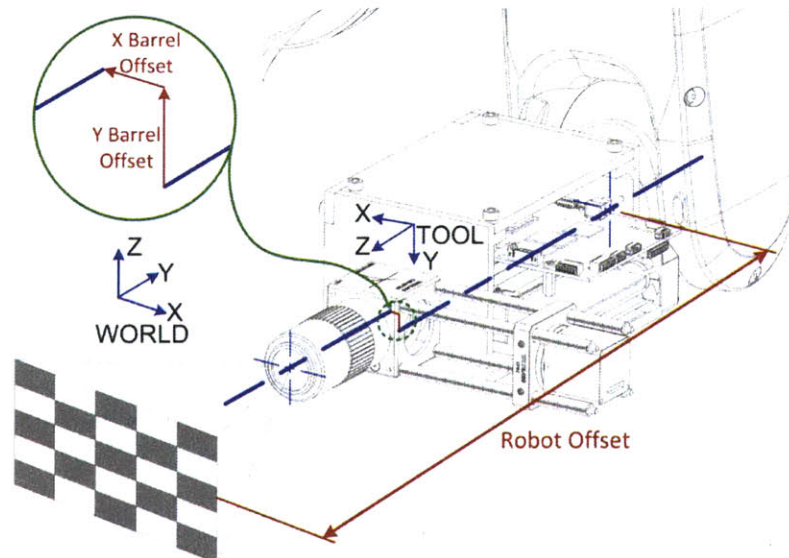


Figure 27: Visualization of the barrel offset and robot offset variables. The barrel offset variables are present to account for manufacturing and assembly misalignment, whereas the robot offset variable is required to keep the projection in focus.

Runout Reduction

The final calibration step is to correct rotary stage runout—the deviation of an object from rotation about the desired (usually geometric) center—by using a dial indicator. Runout in the system is due to misalignment between the workpiece Z axis (as defined in the OBJ file) and the rotary stage axis of rotation. A precision-ground cylindrical pin mounted in the center of a custom kinematic coupler plate is used in conjunction with a dial indicator and orthogonal micrometer stages to bring runout to $\pm 12\mu\text{m}$. Runout is eliminated by the following iterative process:

1. The rotary stage is turned until the dial indicator is parallel with either of the manual micrometer stages.
2. The difference of the dial indicator reading at this position and after rotating the stage 180° is divided by two and applied to the micrometer stage in the direction that reduces the maximum of the two readings.
3. The rotary stage is then rotated 90° and the process is repeated with the dial indicator aligned with the other micrometer stage.
4. Steps 2 and 3 are repeated until the measured runout is within $\pm 12\mu\text{m}$. Runout will then be removed from all workpiece/kinematic coupler assemblies if the workpiece OBJ file Z axis is collinear with the geometric central axis of the digital representation of the kinematic coupler.

CONCLUSIONS

A system composed of an articulated six-axis robot, a rotary stage, and a DLP projection lithography end effector was described, with functionality coordinated by custom software implemented in C++. Two different projection lithography end effectors were designed and details of each were reported. The resolution range between the two end effectors spans approximately one order of magnitude (10-220 μm) and the field of view spans approximately three orders of magnitude (0.12-327 cm^2).

The robotic motion system was selected by considering functional requirements for work envelope, payload capacity, and repeatability. An Adept Viper s650 articulated 6-axis robot was selected based on this analysis.

To pattern freeform surfaces, an operational procedure was developed involving 3D scanning the workpiece using a commercially available laser scanner, applying a computer graphics texture to the digital surface, and registering the digital surface with the physical workpiece in the workcell via a calibration process.

Homogeneous transform matrices were used to model the system as a serial kinematic chain for error estimation via perturbation analysis. The end effector positioning error was estimated to be 650 μm , with the largest single contributor (180 μm) attributed to robot joint 1 due to the increased distance for propagation of sine errors between joint 1 and the end effector.

The following chapter will discuss the patterning performance and observed motion system errors.

intentionally blank

intentionally blank

Chapter 4: System Characterization and Demonstration

This chapter characterizes the lithographic resolution and positioning performance of the robotic lithography system and presents demonstrations of freeform patterning. Based on the magnitude of the measured positioning error, the system was adapted to patterning macro-scale objects in order to reduce the error magnitude as compared to each individual projection. Demonstrations were performed on macroscale surfaces of both positive and negative curvature.

MEASUREMENT OF PROJECTION LITHOGRAPHY RESOLUTION

The resolution of both projection lithography end effectors described in Chapter 3 was evaluated by fabricating a photoresist test pattern. Photoresist is a chemical that undergoes a change in solubility to a solvent after exposure to radiation.¹⁴² Chemically, the solubility response is based on radiation-induced polymer chain formation, scission, or reduction of dissolution inhibition species in the resist. The latter, for example, being the method behind the operation of Novolak resin, a type of phenolic resin.^{143,144} There are a variety of commercially available photoresists on the market, classified into two broad categories called positive and negative photoresist. Positive photoresist directly replicates the solid pattern found on the mask, whereas negative photoresist captures the opposite of the mask pattern.¹⁴⁵ Figure 28 schematically shows the difference between the two photoresist categories. Within each category, there is a variety of photoactive chemistries that have been developed. Two photoresists are used here for testing: an aerosol-based phenolic resin formulation and a photoactive hydrogel, as noted Table 6.

Table 6: The two photopolymer chemistries used.

Photoresist	Type	Application Method	Developer
MicroChem	Positive	Aerosol spray	0.1N NaOH (aq)
MicroSpray – Novolak			
Poly (ethylene glycol) diacrylate (PEG-DA)	Negative	Pipetting	Isopropanol

The MicroSpray aerosol resist is used to conformally coat complex surfaces. The high viscosity of the photoresist prevents flow off of inclined surfaces and enables extended experiments. In addition, the

phenolic resin formulation makes the photoresist resistant to damage after patterning during handling and characterization.

Poly (ethylene glycol) diacrylate (PEG-DA) hydrogel is a biocompatible material that is crosslinked upon exposure when mixed with a photoinitiator, for example Irgacure 819 (Phenylbis (2,4,6-trimethylbenzoyl)-phosphine oxide). The PEG-DA mixture was chosen as a potential support for patterning living cells encapsulated in a viable support material.

Aerosol-based resist is applied as follows. The can is shaken approximately 10 times and sprayed once away from the substrate to clear the nozzle. Next, three quick overlapping passes are sprayed onto the substrate to deposit approximately 5 μm of photoresist, based on optical microscopy measurements. The substrate sits for 5 minutes at room temperature and is then warmed with a hot air gun set to 116 C° for 5 minutes.¹³² Exposure was determined experimentally to be 1.9s for the microscope objective optics and 7 minutes for the wide-angle lens optics. The exposure development time was determined by experimenting with different times and observing the pattern quality via scanning electron microscopy.

Hydrogel application is performed by dipping the substrate into a 100 ml beaker or by manually pipetting 1-10 ml onto the surface, depending on the size of the substrate. Layer thickness will vary with substrate material and frequency of manual pipetting, with layer thickness up to 100 μm having been observed after pipetting 3mL onto a stainless steel substrate. Poly (ethylene glycol) diacrylate hydrogel cures in 1 minute, based on when the photoinitiator concentration is 2g/100mL, with either optics configuration. Exposure development time was determined by experimenting with different times and observing the pattern quality via scanning electron microscopy.

Both the MicroSpray and the PEG-DA resists were applied to glass substrates (uncoated soda lime glass, VWR catalog number 16004-422) and patterned using a USAF 1951 resolution test target photomask.¹⁴⁶ Figure 29 shows the resolution test results for both Novolak aerosol-based photoresist and PEG-DA photoresist using the objective-lens end effector. The results show that with MicroSpray resist a corner-radius resolution of 5 μm in a 5 μm thick layer was achieved. The same experiment was performed using PEG-DA and resulted in a larger corner radius of 15 μm . This is likely due to the PEG-DA layer thickness of approximately 100 μm , which is a result of the dropwise application method.

The USAF resolution test also provides a method for determining the line pair resolution of the projection lithography system. By measuring the smallest resolvable line group (Figure 30), the resolving power was found to be 0.1 lines/ μm , or 10 μm lines.

Figure 31 shows the results of the resolution test performed using the wide-angle lens projection lithography system for the Novolak-based photoresist. The measured corner radius was 400 μm . Difficulty

focusing this optical projection unit without a coaxial CCD limits the focus quality for this projection lithography end effector.

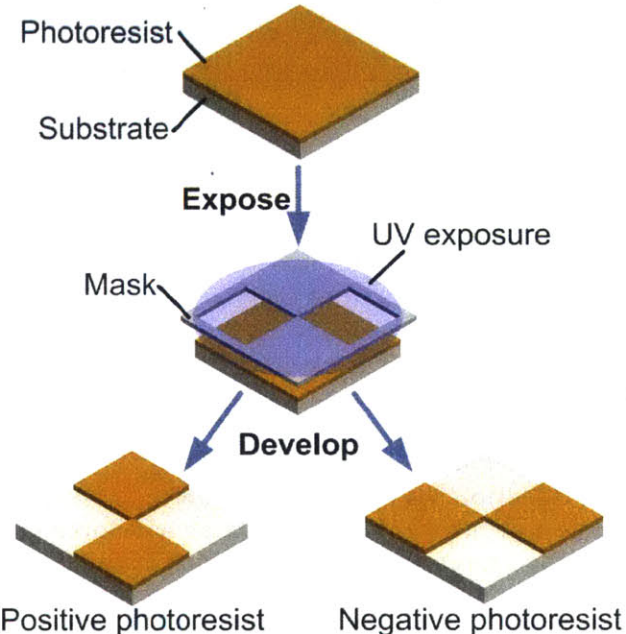


Figure 28: The photoresist patterning process involves uniformly coating a substrate with photoresist, selectively exposing the photoresist using a photomask and light source, and developing the latent image in the photoresist. Positive photoresist directly duplicates the mask pattern, while negative photoresist forms a pattern in the inverse of the mask.

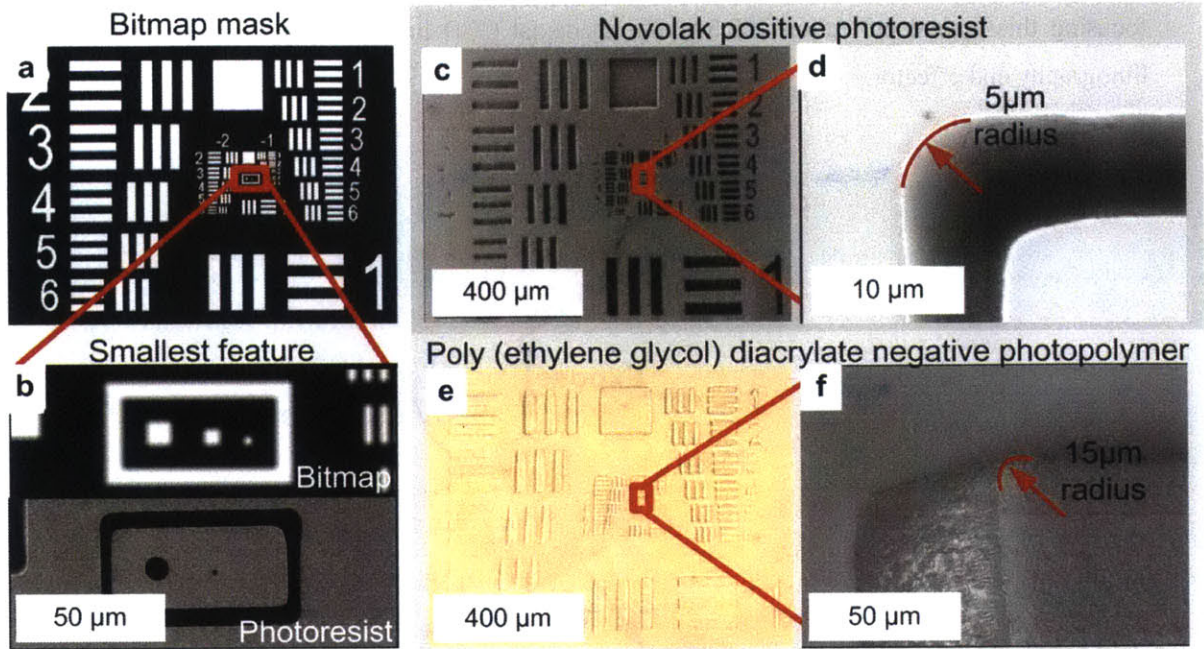


Figure 29: The projection resolution of the objective-lens end effector was tested using a modified version of the 1951 United States Air Force resolution test target. The smallest features in the target are squares that are 3x3, 2x2, and 1x1 pixels in size, respectively, and correspond 1:1 with individual micromirrors in the DMD array. In Novolak positive photoresist, the smallest feature edge radius is 5 μm , and in PEG-DA hydrogel it is 15 μm .

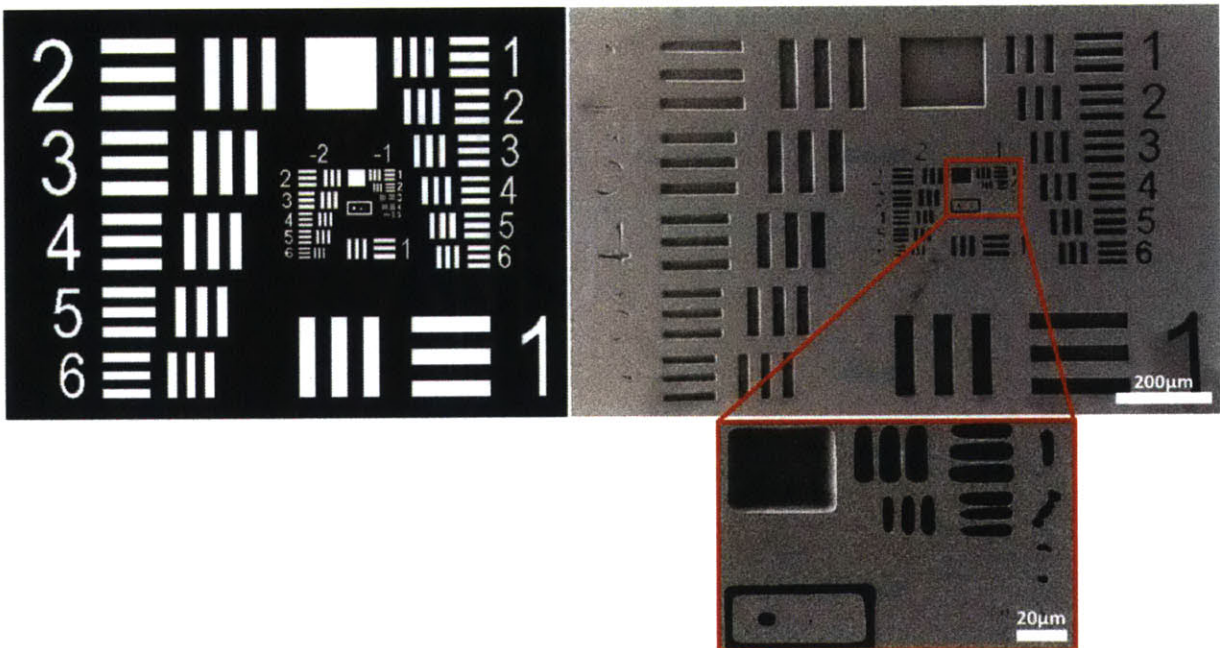


Figure 30: The USAF 1951 test target was used to determine the line pair lithography resolution of the objective lens optics system. The line density (lines/ μm) of the smallest resolvable features is 0.1 lines/ μm , which is equivalent to resolving 10 μm line pairs.

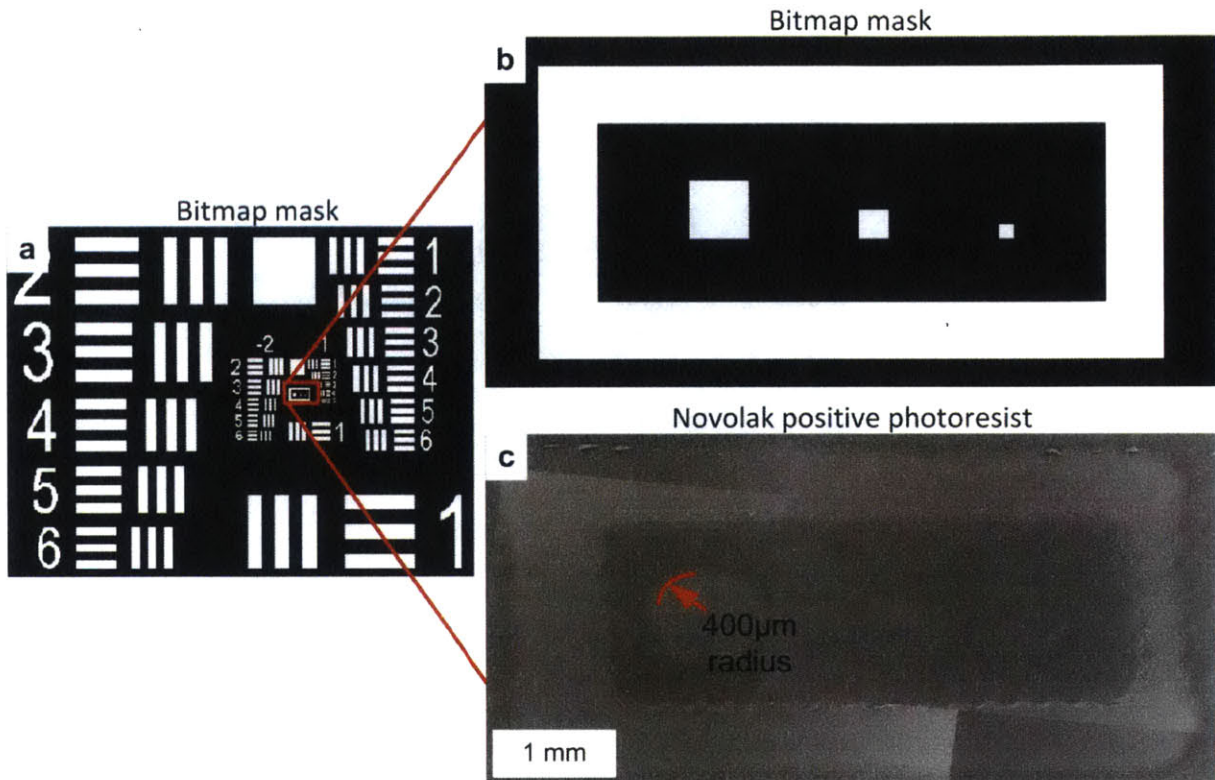


Figure 31: Resolution test of the wide-angle lens end effector: a) The modified 1951 United States Air Force test target bitmap was used; b) The smallest mask features correspond with 3x3, 2x2, and 1x1 patterns of micromirrors in the DMD array; c) Only the 3x3 pixel array fully developed. The radius of curvature for an internal corner is 400µm. Note the SEM micrograph is a composite of several images due to the limited field of view in the microscope.

MEASUREMENT OF THE ACCURACY AND REPEATABILITY OF THE MOTION SYSTEM

The accuracy of the robot in 3D space was measured by patterning triangles on a spherical surface with a radius of curvature of 12.7mm. The triangles were patterned over a partial hemisphere, as shown in Figure 32. The piecewise photomask was overlaid with the result, and by observing triangle placement errors (Figure 33), the accuracy of the system in 3D was estimated (Figure 34).

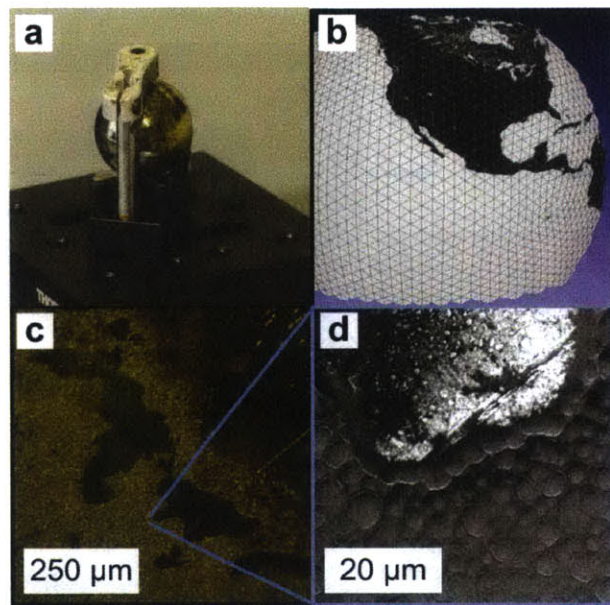


Figure 32: A stainless steel ball bearing was used as a test substrate for the microscope objective projection lithography optics: a) Ball bearing clamped in a v-block on the kinematic coupling; b) Textured OBJ file of the pattern; c) Optical micrograph of pattern in photoresist (orange) on stainless steel (black); d) SEM micrograph of photoresist sidewall—photoresist appears matte and cratered, stainless steel appears reflective.

Figure 34 shows that significant improvements in triangle placement are possible when the positions are corrected by vision feedback. After moving to the location of triangle i , the robot is manually repositioned using the teach pendant in conjunction with visual feedback from the CCD such that triangle i aligns with triangle $i-1$. The now-corrected position is recorded, the photoresist is exposed using blue light, and the cycle repeats for triangle $i+1$. The system can then be re-started using the adjusted triangle coordinates and the triangle tiling accuracy is significantly improved. This demonstrates that the repeatability of the robot is approximately $20\mu\text{m}$, but the accuracy is lower, averaging $330\mu\text{m}$ over this small workspace. When measuring these errors, the resolution of the CCD is the primary limit on the measurement precision.

Using operator feedback to manually correct triangle locations is time intensive. To demonstrate the ability of the system to operate in a coordinated manner without positioning accuracy errors overwhelming the resulting pattern, the wide-angle projection optics end effector was used. In this configuration, the optics field of view is larger while the robot accuracy remains unchanged, therefore the accuracy errors are less as a percentage of the exposure area, and the misalignment won't appear as severe to an observer. In the upcoming demonstrations, the robot measured accuracy error of $330\mu\text{m}$ is approximately 1% of the characteristic length of the projection (a triangle leg measured at 30mm).

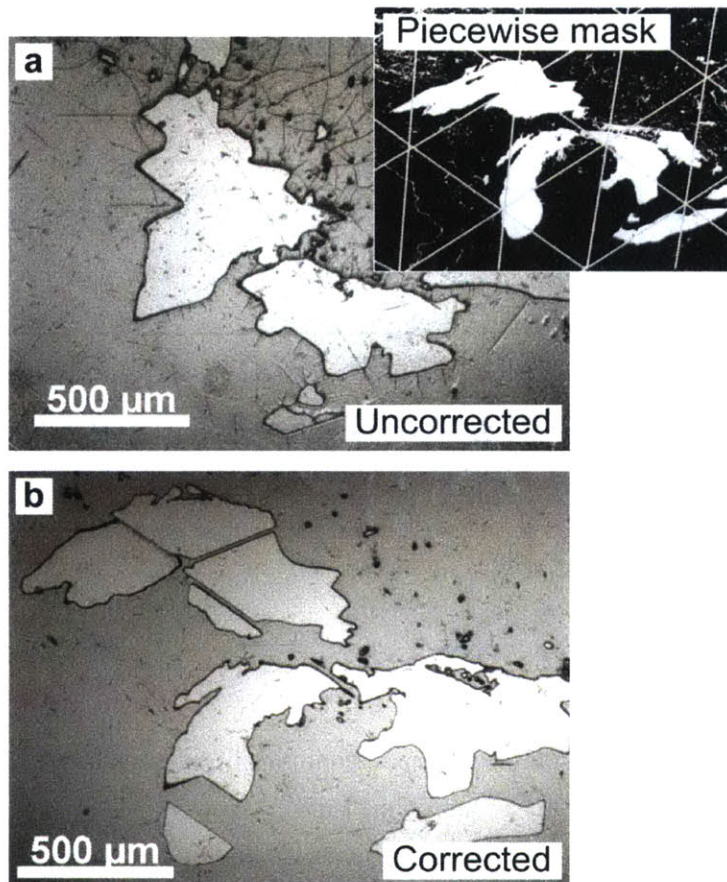


Figure 33: Optical micrographs of a piecewise mask (inset, above-right) developed in MicroSpray Novolak aerosol photoresist: a) At submillimeter length scales, misalignments due to positioning accuracy limitations render overall pattern unrecognizable; b) Using human-operator visual feedback in conjunction with the teach pendant, corrected positions can be calculated and, once calculated, revisited automatically by the robot due to the 20μm system repeatability.

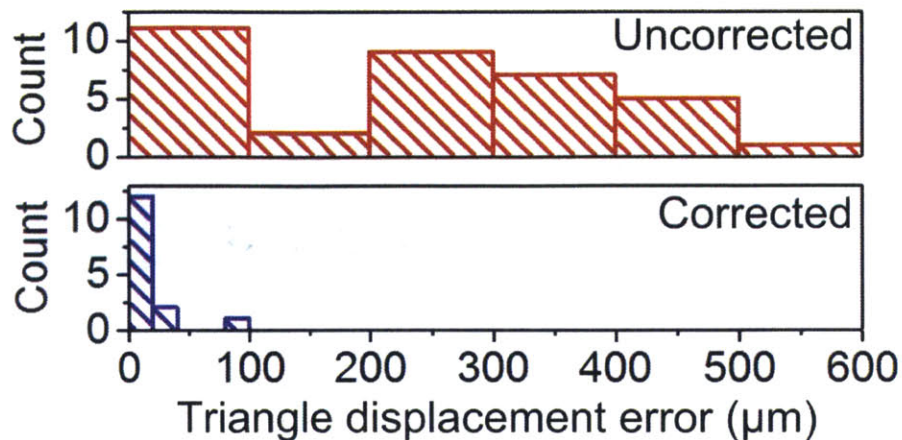


Figure 34: The histogram of triangle placement error between adjacent edges before visual feedback (top), compared to the triangle placement errors after implementing visual feedback (bottom) indicates that the system is capable of 20μm repeatability but only 330μm (on average) accuracy without external correction.

LARGE-SCALE PATTERNING OF A CONSTANT CURVATURE SURFACE

To demonstrate the capability of the system to conformally pattern macroscale 3D objects, a 21.5cm diameter sphere was patterned with a map of the Earth. The workpiece is a white bowling ball with polyurethane outer coating (Brunswick White Viz-A-Ball). MicroSpray Novolak photoresist was applied as described above. Based on experimentation, an exposure time of 7 minutes was used, giving a total cycle time of 9 minutes per triangle, factoring in time consumed by repositioning the motion system between exposures. Motion system repositioning takes 2 minutes since the motion system is moving slowly for safety and in order to allow for the system to settle before exposing. The OBJ file shown in Figure 35 consists of 435 triangular faces, giving an approximate run time of 65 hours. Also seen in Figure 35, the OBJ file for the workpiece was truncated above 60°N and below 20°S due to work envelope limitations. Specifically, the offset required to focus below 20°S latitude would cause the robot end effector to impact the workcell table, and that required to focus above 60°N latitude exceeds the reach of the robot.

The completed workpiece is shown in Figure 36 from several angles. The inset shows the well-defined photoresist boundary and the image of individual micromirrors can be seen in the photoresist, indicating that the focus is maintained while patterning. At high latitudes on the sphere there are small gaps visible between each column of triangles. This is hypothesized to be an alignment error between the physical location of the workpiece and the location described by the ObjectZ offset. Specifically, if the ObjectZ offset indicates that the workpiece is lower than it is in the real world, the patterns will be smaller on top since the robot will be too close and the projected triangles wouldn't have expanded as far given

the fixed numerical aperture of the system. Future work will test this hypothesis. In addition, the few missing triangles visible in Figure 36 are due to a memory overload error in the software that occurred during the extended exposure sequence. The error has since been fixed.

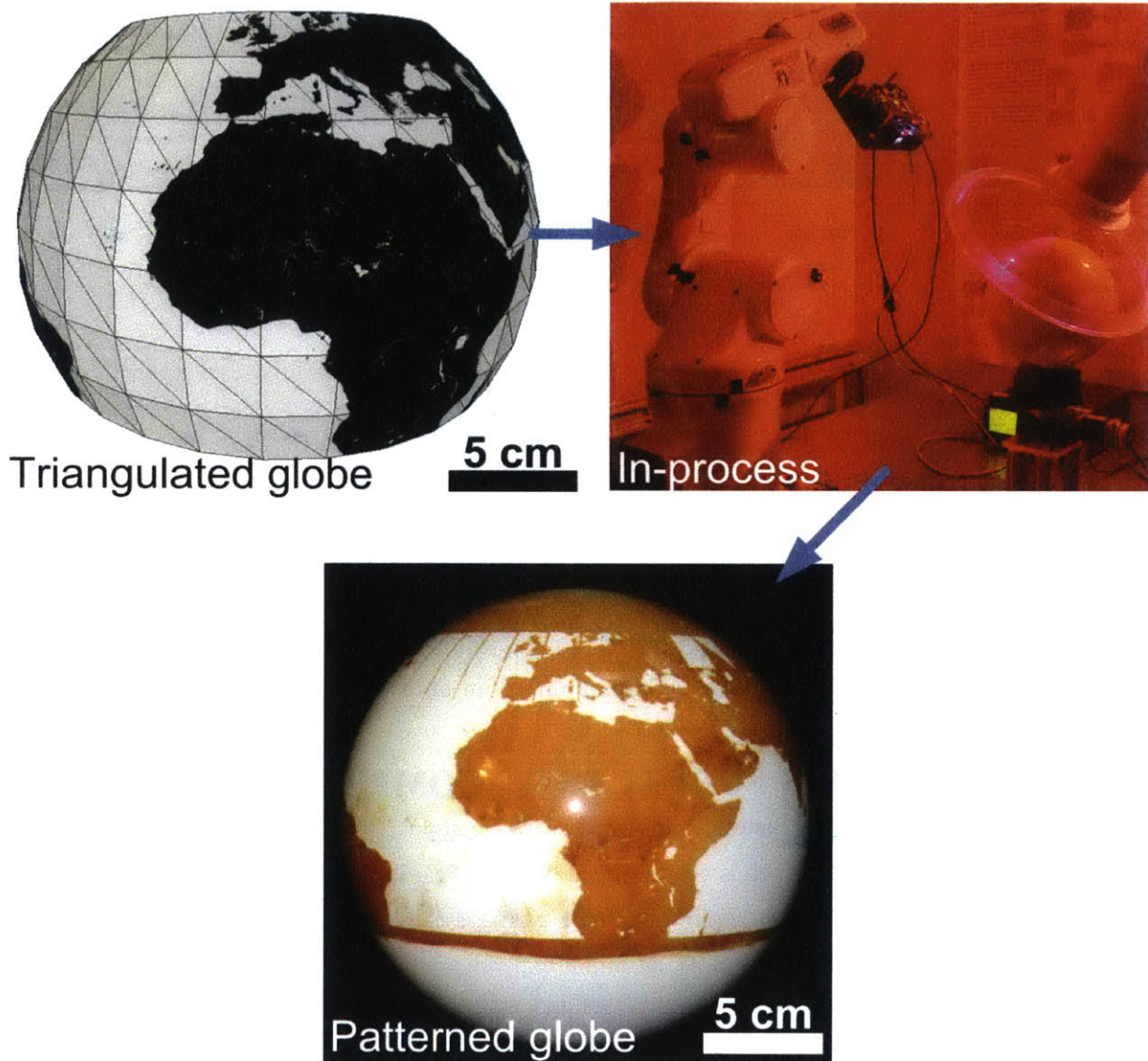


Figure 35: Patterning a macroscale workpiece with a globe map. The upper and lower latitudes of the pattern have been removed due to work envelope limitations.

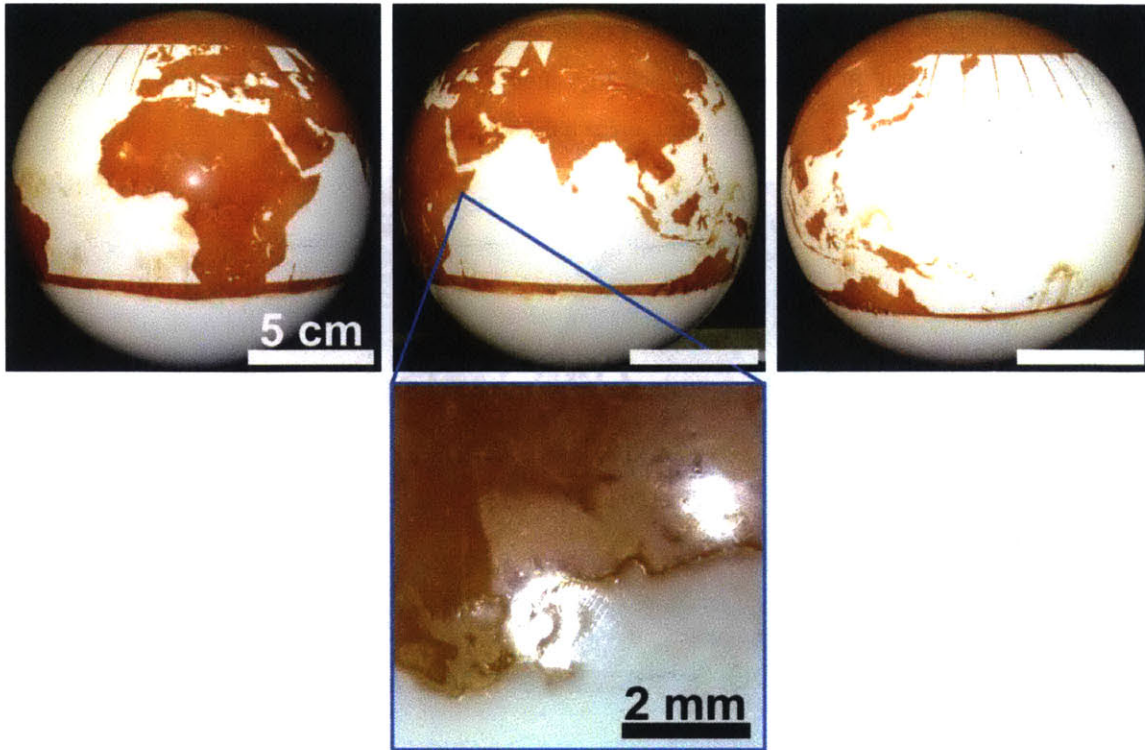


Figure 36: Globe map patterned onto macroscale object. High-magnification view of coastline shows photoresist sidewalls and reveals patterns left by individual micromirrors, demonstrating the minimum possible texture resolution of $220\mu\text{m}$. During development, triangle overlaps of $300\text{-}400\mu\text{m}$ are temporarily visible, corresponding with the measured system accuracy. All scalebars 5cm unless otherwise noted.

PATTERNING ON SURFACES OF COMPLEX CURVATURE

According to the United States Center for Disease Control (CDC), 1 in 3 adults in the United States suffers from osteoarthritis, which is characterized by loss of cartilage in skeletal joints. We are interested in exploring the system as a means of patterning cartilage cells directly on a joint surface or on a 3D model of a patient-specific surface. As an initial experiment, the ability of the system to pattern user-specified objects of arbitrary curvature was investigated, as joint geometry and damage due to osteoarthritis varies patient-to-patient.

Using a NextEngine 3D laser scanner to scan the patellar surface of an anatomical femur model (3B Scientific A35/1R right femur model), an OBJ file was created as shown in Figure 37. The patellar surface model was mounted on the kinematic coupling at the angle shown to more easily access the joint surface with the projection end effector. To ensure proper registration with the system, the OBJ origin was placed in the geometric center of the kinematic coupling top plate as represented in the OBJ file and as defined by the top plate vertical walls defined in the 3D scan (see Figure 37, upper row). As-scanned, the digital workpiece representation contained 1.2 million faces. To reduce cycle time, the mesh was

simplified to 25 faces to allow for patterning to be completed in four hours. A checkerboard pattern containing a gradient of checkers was chosen to test multiple feature sizes simultaneously. Patterning cartilage cells requires the use of the biocompatible PEG-DA, but the initial experiment to test alignment was performed using MicroSpray aerosol-based resist for simplicity.

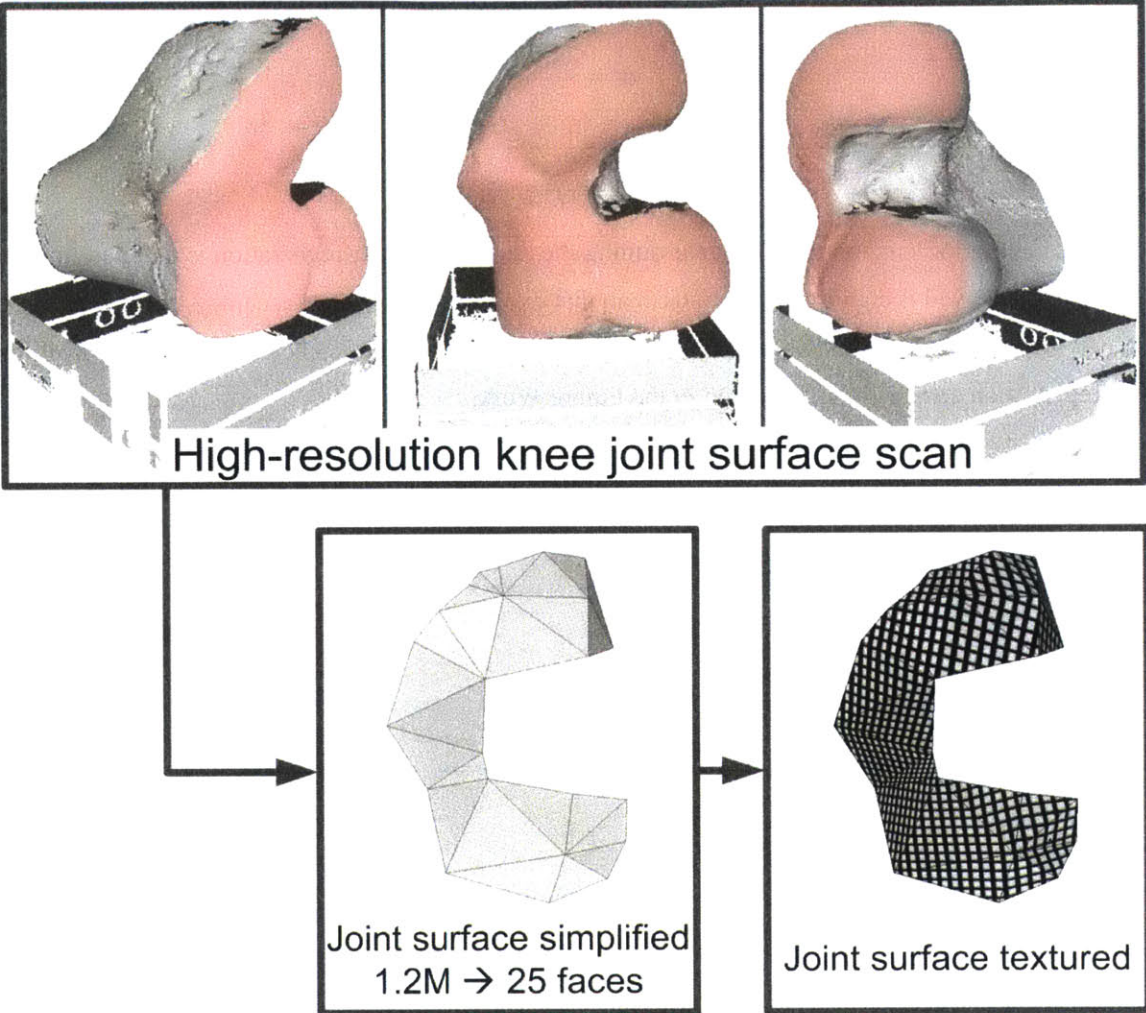


Figure 37: To test the ability to pattern complex curvatures, a femur anatomical model was 3D scanned. The patellar surface is highlighted (top row) to show the region of photoresist patterning. The mesh was simplified from 1.2 million to 25 faces and textured with a simple checkerboard pattern for testing (bottom row).

Results from patterning the femur patellar surface are shown in Figure 38. There are several inter-triangle misalignment errors. The majority of the misalignment is due to rotational alignment error, indicating that the OBJ file was not properly registered with the workpiece. This misalignment is explained in detail in Figure 39. By using a single radius measurement to approximate the local size of the

workpiece (Figure 40), the rotational alignment error that led to this offset can be estimated by the Law of Sines (Eq. 25).

$$\frac{\sin\delta\theta}{\delta x} = \frac{\sin\alpha}{R} \rightarrow \frac{R\sin\delta\theta}{\sin\alpha} = \delta x \quad \text{Eq. 25}$$

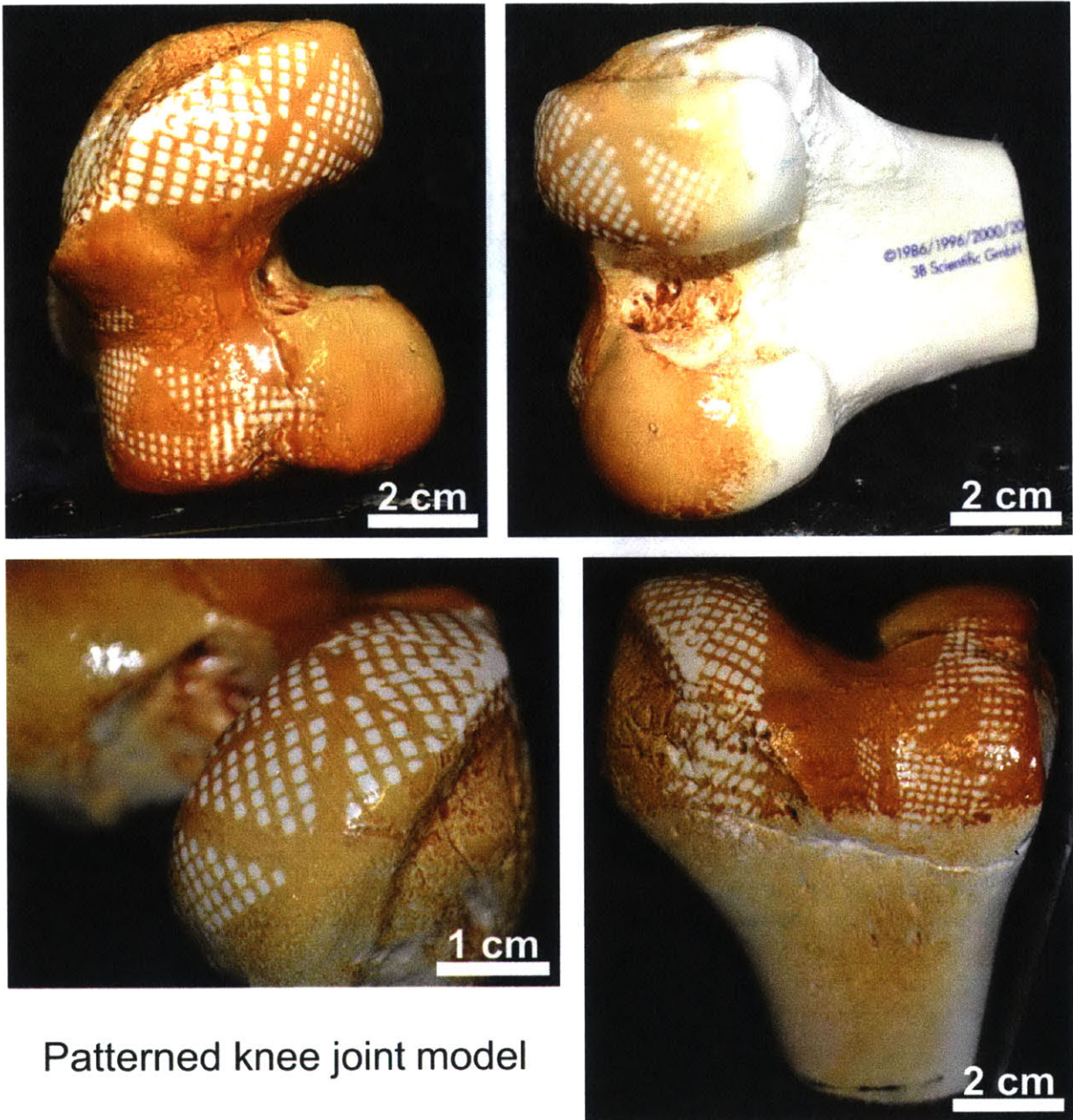
where

$$\alpha = \frac{180^\circ - \delta\theta}{2} \quad \text{Eq. 26}$$

For small angular errors, Eq. 25 becomes

$$R\delta\theta = \delta x \quad \text{Eq. 27}$$

The calibration method used for determining the angle for proper registration is detailed in Figure 41. This error observed is significantly greater than that expected due to robot accuracy, since here the error is due to incorrect calibration, rather than motion system accuracy deficiencies. A method for eliminating this registration error will be discussed in the Future Work.



Patterned knee joint model

Figure 38: The patellar surface patterning test was performed using MicroSpray Novolak photoresist rather than biocompatible poly (ethylene glycol) diacrylate in order to more easily test the system, because the MicroSpray photoresist only needs to be applied once at the beginning of the test. The results indicate that the digital model was not properly registered with the world coordinate frame, causing triangle registry errors.

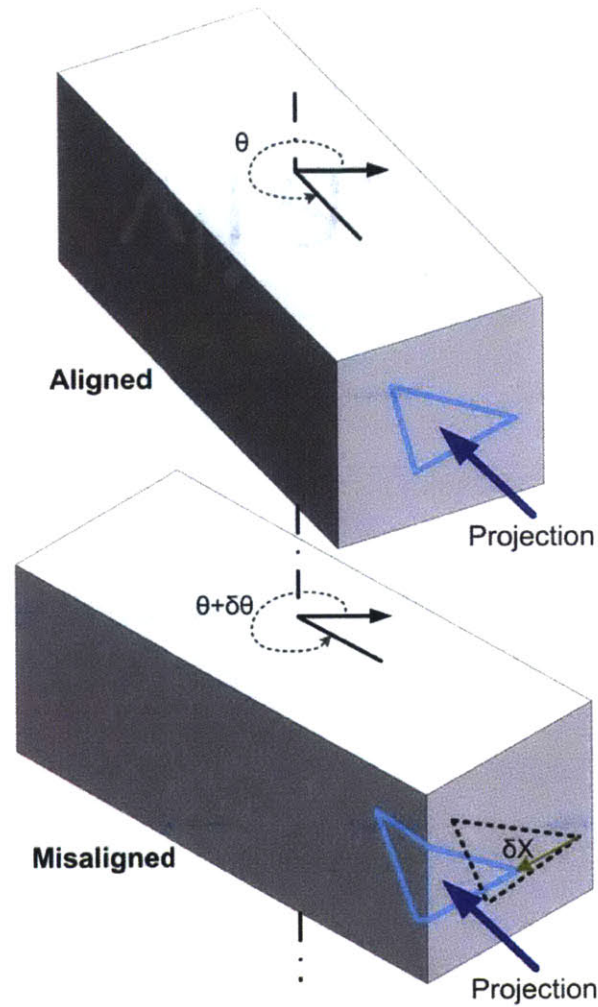


Figure 39: When the workpiece is misaligned relative to the OBJ file by some angle $\delta\theta$, all projected triangles are offset by δX when projected onto the workpiece. In the case of a non-axisymmetric workpiece (such as the femur model), this causes significant deviations in triangle placement.

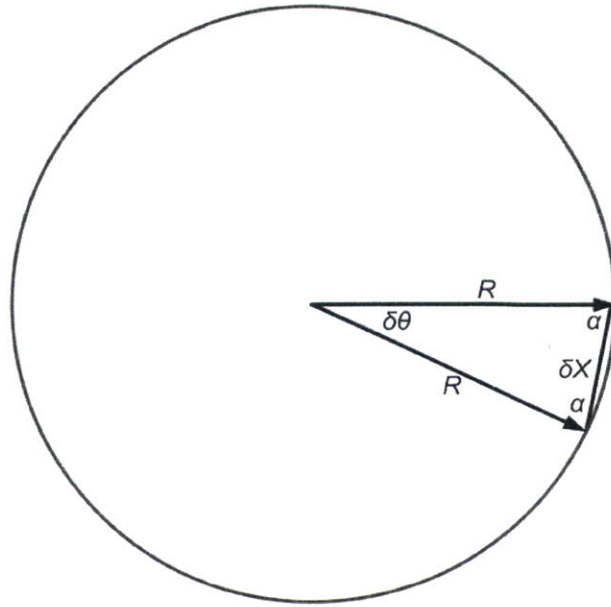


Figure 40: Top view of angular registration error. The local workpiece radius R can be used to estimate the displacement error $\delta\theta$ from a measurement of the displacement error δX using the Law of Sines.

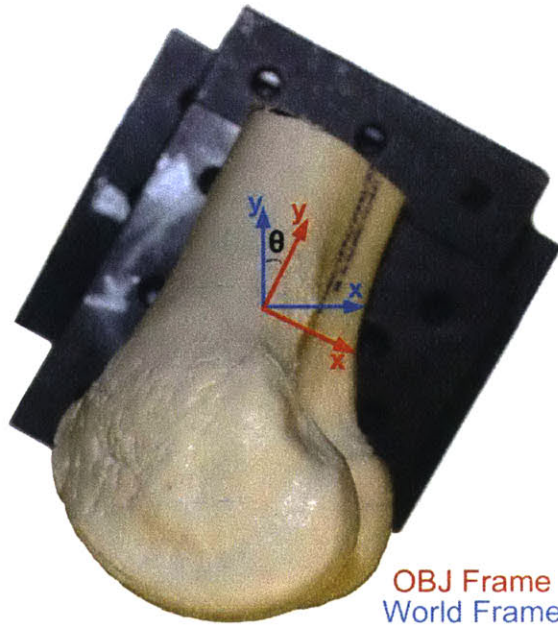


Figure 41: Measurement of the angle required to register a non-axisymmetric object with the world coordinate frame was performed by imaging the mounted workpiece and measuring the angular displacement as shown here. Care must be taken that the image is taken with the CCD orthogonal to the world Z axis, else the measured angular displacement will be incorrect.

This chapter demonstrated the ability of the freeform robotic lithography system to pattern macro-scale objects of user-defined geometry with projection resolving power of $10\mu\text{m}$ and positioning accuracy of $330\mu\text{m}$ over a subset of the robot workspace. Misalignments, when apparent, were discussed in terms of accuracy and calibration errors. Through an investigation into patterning on complex curved surfaces, the application of the system to patterning cartilage onto complex joint surfaces has been explored and will provide areas for future research.

intentionally blank

intentionally blank

Chapter 5: Conclusions and Future Work

This thesis presented the design and construction of a robotic system capable of maskless photopatterning on centimeter- to meter-scale objects. The system incorporates a six-axis serial robot arm, a high-precision rotary stage, a custom-built DLP-based end effector, and custom software that coordinates and controls the system.

Using visual feedback methods, the system positioning accuracy and repeatability over a small region of the working volume was measured at $330\mu\text{m}$ (compared to $650\mu\text{m}$ estimated from the HTM perturbation analysis) and $20\mu\text{m}$, respectively. Accuracy is limited by the design of the robot joint actuators and patterning rate is limited by the power output of the light source. Performance was demonstrated by patterning a 21cm diameter sphere with a map of the Earth. When patterning a complex patellar surface of an anatomical femur model, an angular registration error (described in Figure 39 and Figure 40) caused significant misalignment of the projected texture triangle. The method used to measure the angular offset (Figure 41) is subject to error from out-of-plane misalignment of the CCD with the kinematic coupling.

Therefore, in the future, system positioning performance will be improved by increasing the accuracy of workpiece registration with world coordinates via the use of a portable coordinate measuring machine (CMM) to accurately measure the calibration offsets listed in Table 5. Many commercial portable CMM units have an accuracy of $30\text{-}50\mu\text{m}^{147}$ throughout their 3D working volume, which is significantly more accurate than the manual method involving calipers used earlier. A portable coordinate measuring machine could be mounted in the corner of the work cell and from that position it could be used to measure the displacement vectors in Table 5.

Other opportunities for future work include incorporating machine vision positioning feedback, increasing system patterning rate, and designing and fabricating an additive manufacturing stereolithography end effector to produce graded 3D structures (such as synthetic cartilage) on freeform surfaces.

There are several opportunities for increasing system throughput. Currently the commercially available software used (Meshlab) keeps all triangles approximately equally sized when creating a mesh, regardless of the local curvature. Adapting or creating an algorithm capable of dynamic remeshing as a function of local curvature would increase the system throughput for objects of non-constant curvature, allowing for more efficient utilization of the DLP projection area and increased conformality on highly curved areas..

Consider the depth of field of the system (δ) and the local radius of curvature of the substrate (R). Assuming the local curvature of the substrate can be approximated as spherical, Figure 42 shows the geometric derivation of Eq. 28. The parameter A represents the maximum area of the field of view that can be used for each exposure by taking advantage of the entire depth of field, assuming the local curvature of the substrate can be approximated as spherical.

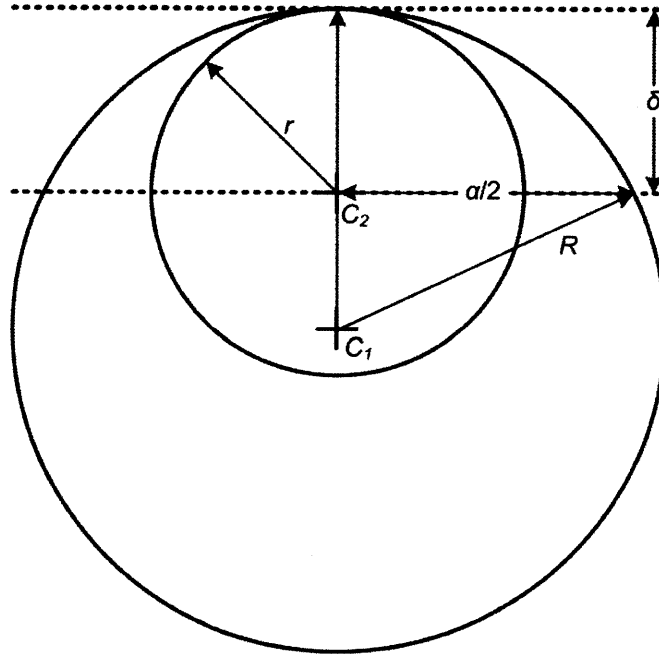


Figure 42: Geometric configuration for the derivation of Eq. 28. Circle C_1 has a radius greater than the depth of field and circle C_2 is the largest circle that will fit an entire hemisphere into the depth of field.

If the radius of curvature is smaller than δ , then A is simply πR^2 . This relationship is plotted in Figure 43c.

$$A = \begin{cases} \pi\delta(2R - \delta) & \text{for } R \geq \delta \\ \pi R^2 & \text{for } R \leq \delta \end{cases} \quad \text{Eq. 28}$$

In such an approach, Eq. 28 could be used to decide the local mesh size when generating the mesh. After measuring the smallest radius of curvature in a given region, A can be calculated to indicate the required triangle size. While we expect this to improve patterning efficiency (measured as percentage of DMD array utilized), there is a tradeoff with processing time as smaller triangles require more exposures to pattern a given area.

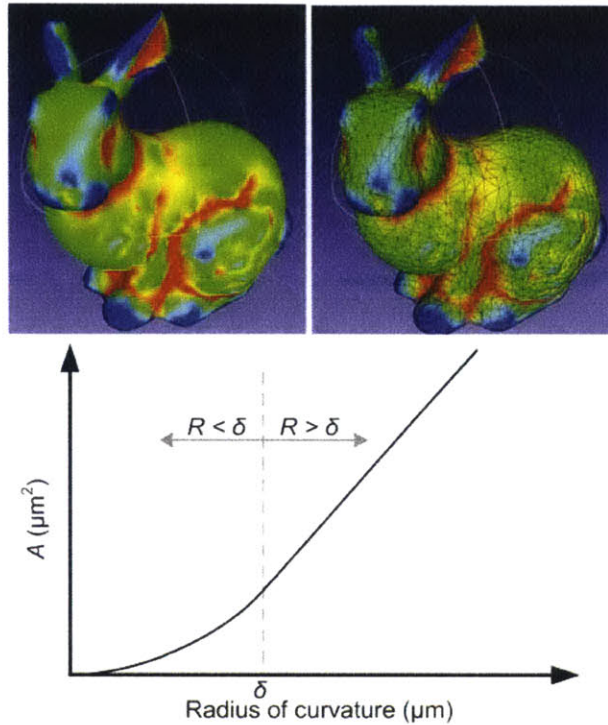


Figure 43: Varying mesh density based on local radius of curvature allows for optimum use of the projection lithography field of view: a) Stanford bunny digital model with surface shaded by local radius of curvature; b) Mesh outline of same; c) Piecewise curve of exposable area (A) as a function of local radius of curvature. Axes are linear.

Throughput would also be increased by increasing the intensity of the light source. Currently the objective and wide-angle projection end effectors operate at 1600 and 0.6 mW/cm², respectively. Increasing the power output would result in an approximately proportional decrease in exposure time, which would significantly reduce system cycle times, because the majority of each cycle is due to exposure time. When designing for increased power intensity, the thermal sensitivity of the micromirror device must be accounted for to prevent overheating and damage to the device from the increased intensity. Options for increased intensity include replacing the current blue led with a higher power LED or modifying the enclosure such that an external standalone light source could supply light via an external fiber light guide.

Finally, there is interest in building graded, three dimensional structures on preexisting freeform surfaces using stereolithography. To achieve this, modified end effector will need to be designed that incorporates a resin delivery system. It is envisioned that this design will enable patterning cartilage cells in user-specified patterns on freeform substrates, such as joint surfaces. A rate analysis co-optimizing curing speed (a function of hydrogel photoinitiator concentration and light intensity) with cell viability will be performed.

intentionally blank

Bibliography

1. Guo N, Leu MC. Additive manufacturing: Technology, applications and research needs. *Front Mech Eng*. 2013;8(3):215–243. doi:10.1007/s11465-013-0248-8.
2. Kodama H. Automatic method for fabricating a three-dimensional plastic model with photo-hardening polymer. *Rev Sci Instrum*. 1981;52(11):1770–1773. doi:10.1063/1.1136492.
3. Hull CW. United States Patent [19] ‘. 1986.
4. Vaezi M, Seitz H, Yang S. A review on 3D micro-additive manufacturing technologies. *Int J Adv Manuf Technol*. 2013;67(5-8):1721–1754. doi:10.1007/s00170-012-4605-2.
5. Kim C., Cuaron a., Perez M a., Espalin D, MacDonald E, Wicker RB. Cooperative Fabrication Methodology for Embedding Wireon Curved Surfaces. *SFF Symp*. 2014:185–196.
6. Goodberlet JG. Patterning 100 nm features using deep-ultraviolet contact photolithography. *Appl Phys Lett*. 2000;76(6):667–669. doi:10.1063/1.125856.
7. Kim JJK, Paik S, Herrault F, Allen MG. UV-LED lithography for 3-D high aspect ratio microstructure patterning. *14th Solid State Sensors, Actuators, Microsystems Work*. 2012:481–484.
8. Schmid H. Light-coupling masks: An alternative, lensless approach to high-resolution optical contact lithography. *J Vac Sci Technol B Microelectron Nanom Struct*. 1998;16(6):3422. doi:10.1116/1.590471.
9. Fang N. Projection Microstereolithography. 2010.
10. Sun C, Fang N, Wu DM, Zhang X. Projection micro-stereolithography using digital micro-mirror dynamic mask. *Sensors Actuators, A Phys*. 2005;121(1):113–120. doi:10.1016/j.sna.2004.12.011.
11. Musgraves JD, Close BT, Tanenbaum DM. A maskless photolithographic prototyping system using a low-cost consumer projector and a microscope. *Am J Phys*. 2005;73(10):980. doi:10.1119/1.1924491.
12. Pease RFW. Electron beam lithography. *Contemp Phys*. 1981;22(3):265–290. doi:10.1080/00107518108231531.
13. Broers AN, Hoole Andrew C.F a. CF, Ryan JM. Electron beam lithography - Resolution limits. *Microelectron Eng*. 1996;32(1-4 SPEC. ISS.):131–142. doi:10.1016/0167-9317(95)00368-1.
14. Brown WL, Venkatesan T, Wagner a. Part IV New uses of ion beams: ion beam lithography. *Nucl instruments methods*. 1981;191:157–168.
15. Watt F, Bettiol A, Van Kan J, Teo E, Breese M. Ion Beam Lithography and Nanofabrication: A Review. 2005;4(3):269–286.

16. Chan Y-C. Development and applications of a laser writing lithography system for maskless patterning. *Opt Eng.* 1998;37(9):2521. doi:10.1117/1.601760.
17. Koch J, Fadeeva E, Engelbrecht M, et al. Maskless nonlinear lithography with femtosecond laser pulses. *Appl Phys A Mater Sci Process.* 2006;82(1 SPEC. ISS.):23–26. doi:10.1007/s00339-005-3418-7.
18. Xia Y, Whitesides GM. Soft Lithography. *Annu Rev Mater Sci.* 1998;28(1):153–184. doi:10.1146/annurev.matsci.28.1.153.
19. Unger M a, Chou HP, Thorsen T, Scherer a, Quake SR. Monolithic microfabricated valves and pumps by multilayer soft lithography. *Science.* 2000;288(5463):113–116. doi:10.1126/science.288.5463.113.
20. Paul KE, Prentiss M, Whitesides GM. Patterning spherical surfaces at the two-hundred-nanometer scale using soft lithography. *Adv Funct Mater.* 2003;13(4):259–263. doi:10.1002/adfm.200304255.
21. Jin H-C, Abelson JR, Erhardt MK, Nuzzo RG. Soft lithographic fabrication of an image sensor array on a curved substrate. *J Vac Sci Technol B Microelectron Nanom Struct.* 2004;22(5):2548. doi:10.1116/1.1795249.
22. Chung HJ, Sulkin MS, Kim JS, et al. Stretchable, multiplexed pH sensors with demonstrations on rabbit and human hearts undergoing ischemia. *Adv Healthc Mater.* 2014;3(1):59–68. doi:10.1002/adhm.201300124.
23. Petruczok CD, Gleason KK. Initiated Chemical Vapor Deposition-Based Method for Patterning Polymer and Metal Microstructures on Curved Substrates. *Adv Mater.* 2012;24(48):6445–6450. doi:10.1002/adma.201201975.
24. Kong YL, Tamargo IA, Kim H, et al. 3D Printed Quantum Dot Light-Emitting Diodes. 2014.
25. Aiscent Technologies. 2015. Available at: <http://www.aiscenttech.com/en/solutions/sphericallylithography/>.
26. Heininger N, Laser L, Ag E. 3D LDS Components for New Production Opportunities. 2015:5–9.
27. Van Kessel PF, Hornbeck LJ, Meier RE, Douglass MR. A MEMS-based projection display. *Proc IEEE.* 1998;86(8):1687–1704. doi:10.1109/5.704274.
28. Milionis A, Bayer IS, Fragouli D, Brandi F, Athanassiou A. Combination of Lithography and Coating Methods for Surface Wetting Control. In: ; 2013. doi:10.5772/56173.
29. Stevens KR, Ungrin MD, Schwartz RE, et al. InVERT molding for scalable control of tissue microarchitecture. *Nat Commun.* 2013;4(May):1–10. doi:10.1038/ncomms2853.
30. Okuma - 5 Axis CNCs. Available at: <http://www.okuma.com/five-axis-cnc-machines>. Accessed January 1, 2015.

31. Motoman Painting Robots. Available at: <http://www.motoman.com/products/robots/painting-robots.php>. Accessed January 1, 2015.
32. Kawasaki - Robotic Material Handling. Available at: https://robotics.kawasaki.com/en/applications/robotic-material-handling/?language_id=1. Accessed January 1, 2015.
33. iRobot - For the Home. Available at: <http://www.irobot.com/For-the-Home.aspx>. Accessed January 1, 2015.
34. Camarillo D, Krummel T, Salisbury J. Robotic Technology in Surgery: Past, Present, and Future. *Am J Surg*. 2004;188(4A):2S–15S.
35. Jiang BC, Black J., Duraisamy R. A review of recent developments in robot metrology. *J Manuf Syst*. 1988;7(4):339–357. doi:10.1016/0278-6125(88)90044-1.
36. Manseur R, Doty KL. Structural kinematics of 6-revolute-axis robot manipulators. *Mech Mach Theory*. 1996;31(5):647–657. doi:10.1016/0094-114X(95)00092-D.
37. Uicker JJ, Denavit J, Hartenberg RS. An Iterative Method for the Displacement Analysis of Spatial Mechanisms. *J Appl Mech*. 1964;31(2):309. doi:10.1115/1.3629602.
38. Velmex - Motor Driven Rotary Tables. Available at: http://www.velmex.com/motor_rotary_tables.html. Accessed January 1, 2015.
39. Omega - Stepper Motors. Available at: http://www.omega.com/pptst/OMHT_SERIES.html. Accessed January 1, 2015.
40. Hagood NWI, McFarland AJ. Modeling of a piezoelectric rotary ultrasonic motor. *IEEE Trans Ultrason Ferroelectr Freq Control*. 1995;42(2):210–224. doi:10.1109/58.365235.
41. Uchino K. Piezoelectric Ultrasonic Motors: Overview. *Smart Mater Struct*. 1998;7:273–285. doi:10.1177/1045389X9500600110.
42. Physik Instrumente - Piezomotor Rotation Stages. Available at: <http://www.physikinstrumente.com/products/precision-rotation-stages.html>. Accessed January 1, 2015.
43. Velmex - Lead Screw Slides. Available at: http://www.velmex.com/manual_sizes.html. Accessed January 1, 2015.
44. Thomson Linear - Ball Screws. Available at: http://www.thomsonlinear.com/website/com/eng/products/ball_screws_and_lead_screws/ball_screws.php. Accessed January 1, 2015.
45. PI USA - Piezo Actuators. Available at: <http://www.pi-usa.us/products/PiezoActuators/>. Accessed January 1, 2015.

46. Global Spec - Rack & Pinion Information. Available at: http://www.globalspec.com/learnmore/motion_controls/power_transmission/gears/rack_pinion_gears. Accessed January 1, 2015.
47. Boldea I, Nasar SA. Linear Electric Actuators and Generators. In: *IEEE.*; 1997:1–5.
48. Hale LC. Principles and Techniques for Designing Precision Machines. 1999.
49. Rotary Table Photograph. Available at: <http://www.intellidrives.com/rotary-table-RotoRing.HTM>.
50. Stepper Motor Photograph. Available at: <http://store.amberspyglass.co.uk/40mm-nema17-stepper-motor-200step-per-rev.html>.
51. Ball Screw Photograph. Available at: http://www-mdp.eng.cam.ac.uk/web/library/enginfo/textbooks_dvd_only/DAN/threads/mechanics/recircBallB IG.jpg.
52. Lead Screw Photograph. Available at: http://www.roton.com/images/acme_screw.jpg.
53. Rack & Pinion Photograph. Available at: http://img.directindustry.com/images_di/photo-g/rack-pinion-20096-2786531.jpg.
54. Dixon FN. Traveling Crane. 1891.
55. Awtar S, Parmar G. Design of a Large Range XY Nanopositioning System. *J Mech Robot.* 2013;5(May 2013):1–13. doi:10.1115/DETC2010-28185.
56. Paul R. *Robot Manipulators: Mathematics, Programming, and Control - The Computer Control of Robot Manipulators*. Cambridge: MIT Press; 1981.
57. Physik Instrumente USA Miniature Hexapods. 2015. Available at: http://www.pi-usa.us/products/Micropositioning_Stage_Hexapod/hexapod-6-axis-stage.php#mini.
58. Robot Type Table. Available at: <https://www.robots.com/images/robots/robots-types.gif>.
59. Kuka Robot Photograph. Available at: http://img.directindustry.com/images_di/photo-g/articulated-robot-6-axis-heavy-load-industrial-17587-5282019.jpg.
60. Cartesian Gantry Robot Photograph. Available at: <http://www.toshiba-machine.com/Upload/Product/03c599bcaa.jpg>.
61. Delta Robot Photograph. Available at: http://www.mdtmag.com/sites/mdtmag.com/files/legacyimages/ABB_Robotics.jpg.
62. Stewart Platform Robot Photograph. Available at: <https://d2t1xqejof9utc.cloudfront.net/pictures/files/814/large.jpg?1324370916>.

63. Kuka Robotics. Available at: http://www.kuka-robotics.com/en/products/industrial_robots/small_robots/kr6_r700_fivve/start.htm. Accessed January 1, 2015.
64. Kuka Robotics. Available at: http://www.kuka-robotics.com/en/products/industrial_robots/special/palletizer_robots/kr1000_1300_titan_pa/start.htm. Accessed January 1, 2015.
65. Kuka Robotics. Available at: http://www.kuka-robotics.com/en/products/industrial_robots/low/kr5_arc/start.htm. Accessed January 1, 2015.
66. Kuka Robotics. Available at: http://www.kuka-robotics.com/en/products/industrial_robots/low/kr6_2/start.htm. Accessed January 1, 2015.
67. Kuka Robotics. Available at: http://www.kuka-robotics.com/en/products/industrial_robots/low/KR_16_3S/start.htm. Accessed January 1, 2015.
68. Kuka Robotics. Available at: http://www.kuka-robotics.com/en/products/industrial_robots/medium/kr60_3/start.htm. Accessed January 1, 2015.
69. Kuka Robotics. Available at: http://www.kuka-robotics.com/en/products/industrial_robots/medium/kr30_116_2/start.htm. Accessed January 1, 2015.
70. Kuka Robotics. Available at: http://www.kuka-robotics.com/en/products/industrial_robots/high/pro/kr90_r2700_pro/start.htm. Accessed January 1, 2015.
71. Kuka Robotics. Available at: http://www.kuka-robotics.com/en/products/industrial_robots/high/nano/kr120_r1800_nano/start.htm. Accessed January 1, 2015.
72. Kuka Robotics. Available at: http://www.kuka-robotics.com/en/products/industrial_robots/high/ultra/kr210_r3100_ultra/start.htm. Accessed January 1, 2015.
73. Kuka Robotics. Available at: http://www.kuka-robotics.com/en/products/industrial_robots/special/shelf_mounted_robots/kr120_r3900_ultra_k/start.htm. Accessed January 1, 2015.
74. Kuka Robotics. Available at: http://www.kuka-robotics.com/en/products/industrial_robots/heavy/kr1000_titan/kr1000_1750_titan/start.htm. Accessed January 1, 2015.
75. Adept Robotics. Available at: <http://www.adept.com/products/robots/6-axis/viper-s1700d/technical-data>. Accessed January 1, 2015.
76. Adept Robotics. Available at: <http://www.adept.com/products/robots/6-axis/viper-s650/technical-data>. Accessed January 1, 2015.

77. Adept Robotics. Available at: <http://www.adept.com/products/robots/6-axis/viper-s850/technical-data>. Accessed January 1, 2015.
78. Adept Robotics. Available at: <http://www.adept.com/products/robots/6-axis/viper-s1300/technical-data>. Accessed January 1, 2015.
79. Adept Robotics. Available at: <http://www.adept.com/products/robots/linear-modules/python/technical-data>. Accessed January 1, 2015.
80. Adept Robotics. Available at: <http://www.adept.com/products/robots/scara/ecobra-600/technical-data>. Accessed January 1, 2015.
81. Adept Robotics. Available at: <http://www.adept.com/products/robots/scara/ecobra-800/technical-data>. Accessed January 1, 2015.
82. Adept Robotics. Available at: <http://www.adept.com/products/robots/scara/cobra-s350/technical-data>. Accessed January 1, 2015.
83. Adept Robotics. Available at: http://www.adept.com/products/robots/parallel/quattro-s650h/downloads/doc_view/340-datasheet-adept-quattro-s650h-robot?tmpl=component&format=raw. Accessed January 1, 2015.
84. Physik Instrumente. Available at: http://www.pi-usa.us/products/Micropositioning_Stage_Hexapod/hexapod-6-axis-stage.php#mini. Accessed January 1, 2015.
85. Physik Instrumente. Available at: http://www.pi-usa.us/products/PDF_Data/M850_Hexapod_Platform_Parallel_Positioner.pdf. Accessed January 1, 2015.
86. Physik Instrumente. Available at: http://www.pi-usa.us/products/PDF_Data/High_load_Hexapod_Platform_Parallel_Positioner.pdf. Accessed January 1, 2015.
87. Physik Instrumente. Available at: http://www.pi-usa.us/pdf/P-915KWEF_Piezo_Hexapod_Datasheet.pdf. Accessed January 1, 2015.
88. Aerotech AGS1000 Gantry System. Available at: <http://www.aerotech.com/product-catalog/gantries/ags1000.aspx>. Accessed August 18, 2015.
89. Fanuc Robotics - M-1iA. Available at: <http://robot.fanucamerica.com/products/robots/productbyseries.aspx?seriesId=4&robotseries=M-1iA>. Accessed August 18, 2015.
90. Fanuc Robotics - M-2iA. Available at: <http://robot.fanucamerica.com/products/robots/productbyseries.aspx?seriesId=22&robotseries=M-2iA>. Accessed August 18, 2015.

91. Fanuc Robotics - M-3iA. Available at: <http://robot.fanucamerica.com/products/robots/productbyseries.aspx?seriesId=5&robotseries=M-3iA>. Accessed August 18, 2015.
92. ABB Robotics - IRB 360 FlexPicker. Available at: <http://new.abb.com/products/robotics/industrial-robots/irb-360>. Accessed August 18, 2015.
93. Asyriil PocketDelta Robot. Available at: <http://www.asyriil.com/en/products/delta-robots.html>. Accessed August 18, 2015.
94. *Veltru D12H Delta Robot Technical Specifications*.; 2011. Available at: <http://www.veltru.com/dnn01/Portals/0/download/datasheets/VELTRU D12H Datasheet.pdf>.
95. *Veltru D8 Delta Robot Technical Specifications*. Veltru AG; 2011. Available at: <http://www.veltru.com/dnn01/Portals/0/download/datasheets/VELTRU D8 Datasheet.pdf>.
96. Adept Quattro ePLC650H-HS. Available at: https://encrypted-tbn2.gstatic.com/images?q=tbn:ANd9GcRr7-G1NJ6uw5wJVgg_zM3BLGjOkLmIzjK5G81B3qfnc7J6g4BbSA. Accessed January 1, 2014.
97. Robots.com - ABB Robot. Available at: <https://www.robots.com/images/blog/original/abb-irb-6620.jpg>. Accessed January 1, 2014.
98. Robots.com - SCARA Robot. Available at: <https://www.robots.com/images/SCARA Robotics.jpg>. Accessed January 1, 2014.
99. Tao PY, Mustafa SK, Yang G, Tomizuka M. *Robot Work Cell Calibration and Error Compensation--Chp 56 of Handbook of Manufacturing Engineering and Technology*. (Nee AYC, ed.). London: Springer London; 2015. doi:10.1007/978-1-4471-4670-4.
100. Gong C, Yuan J, Ni J. Nongeometric error identification and compensation for robotic system by inverse calibration. *Int J Mach Tools Manuf.* 2000;40(14):2119–2137. doi:10.1016/S0890-6955(00)00023-7.
101. Van Brussel H. Evaluation and Testing of Robots. *CIRP Ann - Manuf Technol.* 1990;39(2):657–664. doi:10.1016/S0007-8506(07)63002-9.
102. Liu Y, Shen Y, Xi N, et al. Rapid robot/Workcell Calibration Using Line-based Approach. *2008 IEEE Int Conf Autom Sci Eng.* 2008:510–515. doi:10.1109/COASE.2008.4626550.
103. Conrad KL, Yih TC. Robotic Calibration Issues: Accuracy, Repeatability and Calibration. *8th Mediterr Conf Control Autom.* 2000;(July):17–19.
104. Gan Z, Tang Q. *Visual Sensing and its Applications - Integration of Laser Sensors to Industrial Robots*. Springer; 2011.
105. FANUC Robotics - Automotive Assembly. Available at: <http://robot.fanucamerica.com/fanuc-portal/portal-pages/automotive-assembly-robot-vision.aspx>.

106. NKM Noell Special Cranes GmbH. Available at: <http://www.nkmnoell.com/>.
107. NKM Noell Industrial Cranes. Available at: <http://www.nkmnoell.com/activities/industry/steel/>.
108. Booth N. Press Release. 2015;(March 2014):1–7.
109. Booth N. BAAM Specifications. 2015:1–6.
110. BAAM. Available at: <http://www.e-ci.com/baam>. Accessed January 1, 2015.
111. Printed Shelby Photograph. Available at: <http://energy.gov/eere/articles/secretary-moniz-tours-3d-printed-shelby-cobra>. Accessed January 1, 2015.
112. Viridis3D Robotic Additive Manufacturing RAM260 3D Printing System Brochure. 2015.
113. Viridis3D. Available at: <http://www.viridis3d.com/>. Accessed January 1, 2015.
114. Ford creates sheet metal prototypes in hours instead of weeks. 2015. Available at: <http://www.gizmag.com/ford-f3t/28148/pictures#4>.
115. Everett J, Slocum A. Automation and Robotics Opportunities: Construction versus Manufacturing. *J Constr Eng Manag*. 1994;120(2):443–452.
116. Lim S, Buswell R a., Le TT, Austin S a., Gibb a. GF, Thorpe T. Developments in construction-scale additive manufacturing processes. *Autom Constr*. 2012;21(1):262–268. doi:10.1016/j.autcon.2011.06.010.
117. Ackerman BE. Robots Build Large Structures With Brick and Concrete. 2015:6–7.
118. Yu SN, Ryu BG, Lim SJ, Kim CJ, Kang MK, Han CS. Feasibility verification of brick-laying robot using manipulation trajectory and the laying pattern optimization. *Autom Constr*. 2009;18(5):644–655. doi:10.1016/j.autcon.2008.12.008.
119. Slocum AH, Schena B. Blockbot: A robot to automate construction of cement block walls. *Rob Auton Syst*. 1988;4(2):111–129. doi:10.1016/0921-8890(88)90020-6.
120. Hiller J, Lipson H. Tunable Digital Material Properties for 3D Voxel Printers. In: *19th Annual Solid Freeform Fabrication Symposium*. Austin, TX; 2008.
121. Hiller J, Lipson H. Design and analysis of digital materials for physical 3D voxel printing. *Rapid Prototyp J*. 2008;15(2):137–149. doi:10.1108/13552540910943441.
122. Hiller J. Rapid Manufacturing of Digital Materials.
123. Gibson I, Rosen DW, Stucker B. *Additive Manufacturing Technologies*.; 2010. doi:10.1007/978-1-4419-1120-9.
124. PA-4 Power Supply Image. Available at: Adept.com. Accessed August 4, 2015.

125. SmartController Image. Available at: Adept.com. Accessed August 4, 2015.
126. Adept Viper s650 Robot Image. Available at: <http://www.adept.com/products/robots/6-axis/viper-s650/general>. Accessed August 4, 2015.
127. Stepper Motor Motion Controller Image. Available at: <http://www.allmotion.com/EZHR23ENHCDescription.htm>. Accessed August 4, 2015.
128. Rotary Stage Image. Available at: http://www.velmex.com/motor_rotary_tables.html#6. Accessed August 4, 2015.
129. PC Image. Available at: <http://www.leadwerks.com/workspace/blog/1/entry-1498-the-pc-is-changing/>. Accessed August 4, 2015.
130. Texas Instrument LightCrafter 4500 Image. Available at: TI.com. Accessed August 4, 2015.
131. Slocum AH. Design of three-groove kinematic couplings. *Precis Eng.* 1992;14(2):67–76. doi:10.1016/0141-6359(92)90051-W.
132. MicroChem - MicroSpray Photoresist.
133. *DLP9000FLS 0.9 WQXGA MVSP Type A DMD.*; 2014.
134. Christie Flexible Efficient 3DLP 1080 HD Digital Projector. Available at: <http://www.christiedigital.com/en-us/business/products/projectors/3-chip-dlp/m-series/pages/christie-hd10k-m-dlp-digital-projector.aspx>. Accessed August 13, 2015.
135. AAXA Technologies P4-X Pico Projector. Available at: <http://www.bhphotovideo.com/bnh/controller/home?O=&sku=872139&gclid=Cj0KEQjwgLGuBRCqptLsnJCvh-wBEiQAiNRjsezuPlqLyURNE3Y8AhWMQCbycSLP77PUNmzNx6N5eqcaAstU8P8HAQ&Q=&m=Y&is=REG&A=details>. Accessed August 13, 2015.
136. *DLP LightCrafter 4500 Evaluation Module - User's Guide.*; 2014.
137. Davidson M. Resolution. Available at: <https://www.microscopyu.com/articles/formulas/formulasresolution.html>. Accessed August 14, 2015.
138. Circular Aperture Diffraction. Available at: <http://hyperphysics.phy-astr.gsu.edu/hbase/phyopt/cirapp2.html>. Accessed August 14, 2015.
139. Davidson M. Numerical Aperture. Available at: <https://www.microscopyu.com/articles/formulas/formulasna.html>. Accessed August 14, 2015.
140. Spring K, Davidson M. Useful Magnification Range - Nikon MicroscopyU. Available at: <https://www.microscopyu.com/articles/formulas/formulasmagrange.html>. Accessed August 16, 2015.

141. Adept Viper s650 Technical Data. Available at: <http://www.adept.com/products/robots/6-axis/viper-s650/technical-data>. Accessed August 16, 2015.
142. Bogan LE. The Novolak Synthesis Reaction: A Description Based on Reactivities. *Macromolecules*. 1992;25(7):1966–1969.
143. Bowden MJ, Thompson LF, Fahrenholtz SR, Doerries EM. A Sensitive Novolac-Based Positive Electron Resist. *J Electrochem Soc Solid-State Sci Technol*. 1981;128(6):1304–1313. doi:10.1149/1.2127625.
144. Phenolic Novolac And Resol Resins. Available at: <https://www.plenco.com/phenolic-novolac-resol-resins.htm>. Accessed August 17, 2015.
145. Lithography Overviews - Positive vs. Negative Tone Photoresists. Available at: <http://www.microchem.com/Prod-LithographyOverviewPosNeg.htm>. Accessed August 16, 2015.
146. *T-20 USAF 1951 Chart Standard Layout Product Specifications*. Rochester, New York
147. Hexagon Metrology ROMER Absolute Arm. Available at: <http://www.hexagonmetrology.us/products/portable-measuring-arms/romer-absolute-arm#technical-specifications>. Accessed December 8, 2015.